Nanoelectronics and Its New Materials – A NEW ERA OF NANOSCIENCE

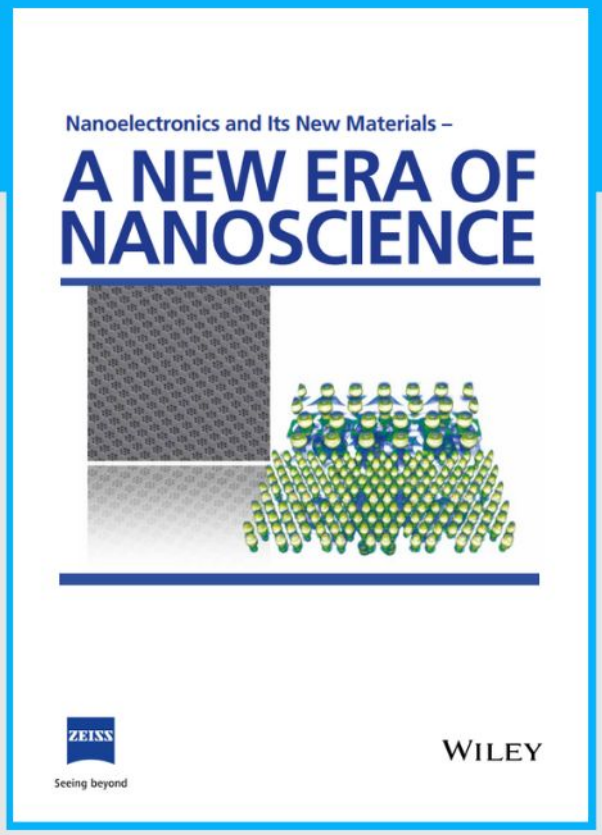

Discover the recent advances in electronics research and fundamental nanoscience.

Nanotechnology has become the driving force behind breakthroughs in engineering, materials science, physics, chemistry, and biological sciences. In this compendium, we delve into a wide range of novel applications that highlight recent advances in electronics research and fundamental nanoscience. From surface analysis and defect detection to tailored optical functionality and transparent nanowire electrodes, this eBook covers key topics that will revolutionize the future of electronics.

To get your hands on this valuable resource and unleash the power of nanotechnology, simply download the eBook now. Stay ahead of the curve and embrace the future of electronics with nanoscience as your guide.

ZEISS

Seeing beyond

WILEY

ADVANCED FUNCTIONAL MATERIALS
www.afm-journal.de

2D Van der Waals Heterostructures for Chemical Sensing

Hui-Lei Hou, Cosimo Anichini, Paolo Samorì,* Alejandro Criado, and Maurizio Prato**

During the last 15 years, 2D materials have revolutionized the field of materials science. Moreover, because of their highest surface-to-volume ratio and properties extremely susceptible to their interaction with the local environment they became powerful active components for the development the high-performance chemical sensors. By combining different 2D materials to form van der Waals heterostructures (VDWHs) it is possible to overcome the drawback of individual materials (such as inertness and zero-bandgap of pristine graphene and less environmental stability of transition metal dichalcogenides). Meanwhile, VDWHs possess unprecedented and fascinating properties arising from the intimate interaction between the components, which can yield superior sensitivities, higher selectivity, and stability when employed to detect gases, biomolecules, and other organic/inorganic molecules. Herein, the latest developments and advances in the field of chemical sensors based on VDWH of 2D materials, with specific insight into the sensing mechanisms, are reviewed and future directions, challenges, and opportunities for the development of the next generation of (bio)chemical sensors with potential impact in environmental sciences and biomedical applications, and more specifically in (bio)chemical defense, industrial safety, food, and environmental surveillance, and medical (early) diagnostics, are discussed.

1. Introduction

The era of the Internet of Things (IoT), via the generation of networks of interconnected devices, represents a unique opportunity for the integration of multiple physical and chemical sensors monitoring health and the environment with the ultimate goal of improving the quality of life. Such sensors can be designed to inspect body movements[1] or detect traces of substances harmful to humans in the air, foods, and water, such as poisonous gases, biomolecules, pesticides, antibiotics, and bacteria.[2,3] Unfortunately, conventional semiconductors-based sensors display some important drawbacks associated with low selectivity and cross-selectivity, lack of mechanical flexibility and foldability, high power consumption, and harsh processing and operating conditions (temperature of 200 to 500 °C).[4] Nowadays, the greatest challenge in chemical sensing is boosting the device selectivity via the exclusive identification and/or detection of the analyte of interest in the presence of other species. Such a task represents a grand challenge in view of the gigantic number of known substances (>10^7) and their chemical similarities in terms of size, surface charges, or structure, and their existence in complex media. Therefore, there is an urgent need to develop new sensing materials possessing excellent comprehensive properties to address the detection requirements in IoT. Significantly, high-performance sensors are highly sought after for applications in various fields, such as personalized medicine (continuous glucose, blood pressure monitoring), and machine brain interfaces (electroencephalograph recording systems, restoring somatosensation), etc.

Generally, the reduction of the dimensionality and the increase of the specific surface area of the sensory materials can naturally amplify their optical, electrical, and (electro)chemical responses. In this regard, low-dimensional nanomaterials (0D, 1D, or 2D) with a high surface-to-volume (or surface-to-mass)

H.-L. Hou, M. Prato
Center for Cooperative Research in Biomaterials (CIC biomaGUNE)
Basque Research and Technology Alliance (BRTA)
Paseo de Miramon 182, 20014 Donostia-San Sebastián, Spain
E-mail: hhou@cicbiomagune.es; prato@units.it

The ORCID identification number(s) for the author(s) of this article can be found under https://doi.org/10.1002/adfm.202207065.

[+]Present address: BeDimensional S.p.A., Via Lungotorrente Secca 30R, Genova 16163, Italy

DOI: 10.1002/adfm.202207065

C. Anichini,[+] P. Samorì
CNRS
ISIS UMR 7006
University of Strasbourg
8 allée Gaspard Monge, 67000 Strasbourg, France
E-mail: samori@unistra.fr

A. Criado
Centro de Investigacións Científicas Avanzadas (CICA)
Universidade da Coruña
Rúa as Carballeiras, 15071 A Coruña, Spain

M. Prato
Department of Chemical and Pharmaceutical Sciences
INSTM UdR Trieste
University of Trieste
Via L. Giorgieri 1, 34127 Trieste, Italy

M. Prato
Ikerbasque
Basque Foundation for Science
48013 Bilbao, Spain

ratio offer higher sensitivity and lower limits of detection (LODs) in chemical sensing when compared to their corresponding bulk (3D) materials.[5,6] Among them, 2D materials with their single or few atomic layer thickness, combined with their outstanding physical and chemical properties, have attracted tremendous worldwide research interest for various applications in (opto)electronics, chemical sensing, energy storage and generation, etc.[7–10]1.1. Properties of 2D Materials Make Them Ideal for Chemical Sensing.

The characteristics of 2D materials are very different from those of their bulk multilayered counterparts.[11,12] Among others, they display, i) good in-plane stability due to the covalent bonds tethering the composing atoms arranged in monolayers and the absence of dangling bonds,[13] for example, the intrinsic strength of the monolayer membrane is 42 N m^{-1},[14] ii) quantum confinement occurring perpendicularly to the 2D plane, leading to unique optical and electrical features,[15] such as high carrier mobility, $\mu > 10^4 cm^2\ V^{-1}\ s^{-1}$ for graphene,[16] and iii) a tunable bandgap,[17,18] e.g., ≈1.2 to ≈1.8 eV for 2H phase MoS_2.[19,20] The high surface-area-to-volume ratio and high density of active surface sites of 2D materials lead to high sensitivity to target analytes. By exploiting the rich surface chemistry, which can be optimized through chemical functionalization or defect engineering, it is possible to achieve good selectivity in the 2D materials-based sensors.[6,21,22] For example, the decoration of the basal plane of graphene with various organic groups and biomolecules acting as receptors of the analyte of interest represents a powerful strategy to improve the specificity in the recognition process resulting in high selectivity of graphene-based sensors.[23–25] The existence of a bandgap in 2D materials, which can be adjusted by using external stimuli such as mechanical force or an electric field, is instrumental in achieving enhanced signal transduction.[26,27]

In view of the outstanding charge transport characteristics of 2D materials that are retained in sub-nanometer thick films, downscaling miniaturized devices has become possible. Moreover, the large lateral size of 2D materials guarantees good electrical contacts in electronic devices.[28] Furthermore, the unique mechanical properties, including their flexibility combined with excellent mechanical strengths, make them particularly suitable for wearable technologies.[29,30] The above-mentioned physical and chemical properties render 2D materials very good candidates for sensing applications. Nowadays, numerous top-down and bottom-up synthetic protocols have been developed and optimized to precisely control the number of layers, lateral size, composition, and overall quality of the 2D material enabling tuning of their specific properties in view of the chosen application. Graphene and transition metal dichalcogenides (TMDs) have been intensively investigated for application in sensing because of their easy accessibility and unique characteristics.[31,32] Until now, most of the literature is based on MoS_2 and graphene since MoS_2 is the most explored 2D material after graphene, and to date VDWH are still in an early stage. In fact, we have included works on other heterostructures such as WSe_2/WS_2, MoS_2/WSe_2, phosphorene/molybdenum diselenide ($MoSe_2$), $NbSe_2/WSe_2$, and graphene/WS_2/graphene, black phosphorus (BP)/WS_2, BP/WSe_2, as summarized in **Tables 1** and **4**.

1.2. Essential Characteristics and Key Performance Indicators (KPIs) in Sensors

Chemical sensors should combine good selectivity, high sensitivity and low LOD, fast response/recovery time, and cyclability (robustness). Selectivity is the capacity to detect the target analyte exclusively among the enormous number of molecular substances, including interfering agents, which may have chemical similarities and isomers. For practical applications, selectivity is, therefore, an insurmountable requirement. Selectivity strongly depends on the kind of interaction existing between 2D materials and target analytes, which can be physical (i.e., physisorption) or chemical (i.e., chemisorption). In addition, the rich chemistry of the surface of 2D materials provides various possibilities to immobilize the receptors through covalent or noncovalent bonds, which further facilitates the specificity in the process of recognition of the analyte, resulting in higher selectivity. Moreover, the cross-reactivity analysis, exposing the sensor to chemically similar species to the target analyte, is essential for demonstrating selectivity, which indicates that the sensor can be used in practical applications.[33] It is also important to differentiate LOD and sensitivity. LOD indicates the theoretical minimum detectable concentration/amount owing to the background noise, which can be calculated by Equation (1).[34] Nevertheless, the value determined experimentally is typically much higher than the effective LOD due to the noise. The sensitivity is defined as the response normalized by the concentration of the analyte, and the response $R(\%)$ as a ratio of the difference between the output of the sensor (e.g., resistance, current) in presence and in absence of the target analyte, over the output in the absence of the target analyte (Equation (2))[35]

$$\mathrm{LOD} = \frac{3\sigma}{S} \tag{1}$$

$$R(\%) = \frac{O(t) - O_0}{O_0} \cdot 100 \tag{2}$$

where σ is the standard deviation of the background (without analyte), S is the slope of the linear relationship between the sensor output signal and the concentration of analyte, $O(t)$ and O_0 are the output of the sensor in the presence and the absence of the target analyte, respectively.

Response/recovery time is another critical indicator for sensors. "Instantaneously" (<1 s) response toward the analyte is ideal for sensors. Physisorption (e.g., π–π interaction) without new covalent bond formation between analyte and sensors as analyte recognition exhibits a faster response than chemisorption. However, biosensors with DNA generally use the covalent bonds to immobilize the receptor. Therefore, it is important to consider the specific application purpose during the development of sensors. Cyclability (robustness) is also important for reusable sensors but not for disposable sensors.

1.3. Advantages and Disadvantages of Individual 2D Materials for Sensing

Graphene and graphene-based materials are considered extraordinary 2D materials and have gained significant attention.[8,24,36]

Table 1. Summary of the VDWHs for gas sensing treated in this section.

Gas sensors						
Heterostructure	Preparation	Sensed molecule[a)]	Sensitivity	LOD	t_{res}, t_{rec}	Refs.
MoS_2/G	CVD (G)/wet transfer	NH_3, (NO_2)	20% @3 ppm	1.2 ppm	5 min, 30 min	[99]
$NbSe_2$/WSe_2	CVD	(NO_2), NH_3, N_2O, CO_2, CO	27% @1 ppm	0.1 ppm	>5 min	[98]
MoS_2/h-BN	Dry transfer	EtOH, MeOH, ACN, ($CHCL_3$), toluene	$10^{5\%}$ @13 kPa		10 min, no rec	[107]
G/h-BN	Wet transfer	NH_3	52% @20%NH3		10 min, 5 min	[108]
MoS_2/hBN	Dry transfer	NH_3, (NO_2)	100% @40 ppm	1 ppm		[109]
MoS_2/hBN	Dry transfer	NO_x		6 ppb	20 s	[110]
G/WS_2/G	Wet transfer	NH_3, (NO_2)	36% @30 ppm	1 ppm		[112]
BP/$MoSe_2$	Dry transfer	NO_2	10.5% @25 ppb	10 ppb	300 s, 50 s	[113]
p-typeMoS_2/n-typeMoS_2	CVD/sol–gel	NO_2	120% @2 ppm	8 ppb	150 s, 30 s	[115]
WSe_2/MoS_2	Dry transfer	(NO_2), TNT	8.19%/ppm	0.15 ppm	385 s, 175 s	[114]
G/MoS_2	CVD (G)/dry transfer	NO_2	1.6×10^5% @1 ppm			[116]
WSe_2/WS_2	CVD	NH_3, (NO_2)	178% @10 ppm			[117]
MoS_2/WSe_2	CVD	(NH_3), NO_2	62% @10 ppm			[117]
MoS_2/WSe_2/MoS_2	Dry transfer	(NH_3), NO_2	1200% @50 ppm		9 s, 17 s	[118]
WSe_2/MoS_2/ WSe_2	Dry transfer	(NO_2), NH_3	1800% @50 ppm		26 s, 14 s	[118]
WS_2/WSe_2	LPE	Humidity	5700% @80%RH		40 s, 65 s	[119]
MoS_2/rGO	LPE	Humidity	872% @50%RH	0.01%RH	6.3 s, 30 s	[120]

[a)]In brackets are reported the gases for which the sensor has the highest sensitivity. The other figures of merit are referred to the gas in brackets. LOD = limit of detection. t_{res} = response time. t_{rec} = recovery time. LPE = liquid phase exfoliation.

In addition, graphene demonstrates distinct advantages for developing sensors, such as a large surface-to-volume ratio, high carrier mobility, and exceptional thermal and electrical properties.[8,23] For example, monolayer graphene possesses the highest reported surface area per gram with a theoretical maximum of 2630 m^2 g^{-1}.[37] The physical adsorption of molecules on the basal plane of the graphene surface causes a significant change in its electrical characteristics, enabling the detection of individual molecules.[38–40] The linear energy-momentum dispersion relationship near the Dirac point of graphene displays a strong broadband absorption from the ultraviolet to infrared region,[41] resulting in different reflectance for transverse electric and transverse magnetic (TM) modes under total internal reflection.[42–44] This difference is sensitive to the media contact's refractive index (RI) with graphene. The RI is a crucial parameter for the sensitivity and resolution of surface plasmon resonance (SPR) sensors. The good conductivity, high current density, and carrier mobility

Table 2. Summary of the VDWHs for electrochemical sensors in this section.

Electrochemical sensors					
Sensing platform	Preparation	Sensitivity	Target	LOD [μM]	Refs.
MoS_2/rGO/GCE	Hydrothermal method	101.70 (μA cm^{-2} mM^{-1})	H_2O_2	0.19	[129]
MoS_2/G-MWCNTs/GCE	Hydrothermal method	5.184 μA μM^{-1} cm^{-2}	H_2O_2	0.83	[130]
MoS_2/rGO/GCE	Hydrothermal method	0.46 μA μM^{-1} cm^{-2}	NO_2^-	0.17	[131]
AuNP/MoS_2/G/GCE	Hydrothermal method	Data not shown	NO_2^-	1.0	[132]
rGO/MoS_2/PEDOT/GCE	Hydrothermal method	874.19 μA μM^{-1} cm^{-2}	NO_2^-	0.059	[133]
3D MoS_2/G/GCE	Hydrothermal and annealing	0.457 μA μM^{-1} cm^{-2}	Methyl parathion	3.2×10^{-3}	[85]
PDDA/G/MoS_2/AuNPs/GCE	Hydrothermal method	Data not shown	Eugenol	0.036	[86]
MoS_2/G/GCE	Hydrothermal method	Data not shown	Ac	0.02	[134]
MoS_2-TiO_2/rGO/SPE	Hydrothermal method	0.4425 μA μM^{-1}	Ac	0.046	[135]
HM-Al^{3+}-(2D-MoS_2)/SPGrEs	Drop-casting	$(1.32 \pm 0.01) \times 10^4$ A cm^2/mol mM	Hydrazine	1.05	[87]
MoS_2/GO/IDEs	Mixture of dispersions	Data not shown	CB, Ery, SS, TH	0.5×10^{-3}[a)]	[136]

[a)]Limit of quantification.

Table 3. Summary of the VDWHs for electrochemical biosensors in this section.

Electrochemical biosensors					
Sensing platform	Preparation	Sensitivity	Target	LOD	Refs.
Nafion/Hb/MoS_2-rGO/GEC	Hydrothermal method	346.6 μA mM^{-1} cm^{-2}	H_2O_2	25 nM	[137]
Mb/MoS_2/GO/Au	Mixture of dispersions	Data not shown	H_2O_2	20 nM	[138]
Mb/MoS_2/GO/Au	Mixture of dispersions	Data not shown	NO	3.6 nM	[141]
Nafion/Mb/MoS_2/Gr/GEC	Mixture of dispersions	Data not shown	H_2O_2	1.25 mM	[142]
Nafion/Mb/MoS_2/G/ GEC	Mixture of dispersions	Data not shown	$NaNO_2$	0.125 mM	[142]
Anti-EpCAM/MoS_2/rGO/ITO	Hydrothermal method	0.104 mA ng^{-1} mL cm^{-2}	EpCAM antigen	44.22 fg mL^{-1}	[143]
3D MoS_2/G aerogels/Gox/GEC	Hydrothermal method	3.36 μA mM^{-1}	Glucose	0.29 mM	[146]
GP/MoS_2/Cu	Hydrothermal method	3.38 mA cm^{-2} mM^{-1}	Glucose	500 nM	[147]
GP/MoS_2/Cu/ lactate oxidase	Hydrothermal method	0.083 mA cm^{-2} mM^{-1}	Lactate	0.1 μM	[147]
Cu_xS/MoS_2/rGO/GCE	Hydrothermal method	308.17 μA mM^{-1} cm^{-2}	glucose	0.6 μM	[148]
rGO/MoS_2/ polyaniline @AuNPs/Apt/GCE	Hydrothermal method	Data not shown	AFB_1	0.002 fg mL^{-1}	[154]
LBA/PEI/rGO/MoS_2/GCE	Mixture of dispersions	Data not shown	LPS	3.01×10^{-5} ng mL^{-1}	[88]
L1/MoS_2/rGO/GCE	Drop-casting	2.35 mA ng mL^{-1} cm^{-2}	HPV	0.1 ng mL^{-1}	[155]
Fe_3O_4NPs/MoS_2/rGO/GCE	Hydrothermal method	Data not shown	MCF-7	6 cells mL^{-1}	[156]
MoS_2/rGO/GCE	Hydrothermal method	0.12 μA μM^{-1} cm^{-2}	AA	0.72 μM	[157]
MoS_2/rGO/GCE	Hydrothermal method	4.11 μA μM^{-1} cm^{-2}	DA	0.05 μM	[157]
MoS_2/rGO/GCE	Hydrothermal method	1.59 μA μM^{-1} cm^{-2}	UA	0.46 μM	[157]
MoS_2/G/GCE	Mechanical transfer	Data not shown	DA	0.5 μM	[158]
MoS_2/G paper	Mixture of dispersions	229.07 mA mM^{-1} cm^{-2}	FA	3.68×10^{-2} μM	[159]

of graphene endow it as a good candidate for field-effect transistors (FETs) sensors, which are worked by monitoring the change of conductance of graphene under target analytes. The conductance of graphene in FET, reflected by charge neutrality point (CNP), sensors is extremely sensitive to molecular adsorptions (both in solution and air) owing to its linear band structure around the K point. Meanwhile, the quantified analysis of FET is dependent on the CNP shift degree. In other

Table 4. Summary of the VDWHs for SPR biosensors in this section.

SPR biosensors				
Sensing platform	Type of work	Sensitivity	Target	Refs.
Ag/MoS_2/G	Theoretical work	105.71° RIU^{-1}	DNA	[166]
Au/MoS_2/G	Theoretical work	87.8° RIU^{-1}	DNA	[167]
Ag/MoS_2/G	Theoretical work	73.5° RIU^{-1}	DNA	[168]
Ag/BP/G	Theoretical work	217° RIU^{-1}	Data not shown	[169]
Ag/BP/MoS_2	Theoretical work	218° RIU^{-1}	Data not shown	[169]
Ag/BP/WS_2	Theoretical work	237° RIU^{-1}	Data not shown	[169]
Ag/BP/$MoSe_2$	Theoretical work	229° RIU^{-1}	Data not shown	[169]
Ag/BP/WSe_2	Theoretical work	279° RIU^{-1}	Data not shown	[169]
Ag/BP/G	Theoretical work	4050 nm RIU^{-1}	DNA	[170]
Au/MoS_2/G	Theoretical work	Data not shown	DNA	[165]
AuNPs/MoS_2/G	Theoretical work	360 nm/RIU	DNA	[172]
Au/G/MoS_2	Theoretical work	5.0 μm RIU^{-1}	Data not shown	[161]
Cu/G/MoS_2	Theoretical work	6.2 μm RIU^{-1}	Data not shown	[161]
Al/G/MoS_2	Theoretical work	6.2 μm RIU^{-1}	Data not shown	[161]
TiO_2/SiO_2/Au/MoS_2/ G	Theoretical work	84.09° RIU^{-1}	Biomolecules	[173]
TiO_2/SiO_2/Au/MoS_2/ G	Theoretical work	85.375% RIU^{-1}	Formaldehyde	[174]
Au/MoS_2/G	Experimental work	6708.87 nm RIU^{-1}	Glucose	[175]

words, the change of CNP is dependent on the chemical environment (such as reaction or adsorption of analytes, and pH change) of graphene in the graphene-based FET.[45,46] The wide electrochemical window (up to 2.5 V) of graphene[47] provides the opportunities for detecting analytes with high reduction or oxidation potentials, and suitable electrocatalytic activities for various redox reactions.[48] It is worth noting that the notorious zero-bandgap of graphene represents a veritable drawback for any application in optoelectronics. This problem can be overcome through the covalent functionalization of graphene to adjust, i.e., opening, the bandgap yet it has the simultaneous disadvantage of reducing its conductivity.

Fortunately, it has been predicted that over 1000 different layered van der Waals (VDW) materials, with a vast diversity in their physical and chemical properties, can be potentially exfoliated.[49] Among them, TMDs are extremely widespread and possess a general chemical formula MX_2, where M is a transition metal (Mo, W, ...) and X is a chalcogen atom (S, Se, or Te).[19] Like graphene, TMDs also possess a large specific area, making them ideal platforms for improving sensor efficiency. In particular, molybdenum disulfide (MoS_2) is the most investigated owing to its abundance in nature. In its 2H phase, it is a semiconductor with a thickness-dependent direct bandgap (≈1.2 to ≈1.8 eV).[19,20] Such characteristic makes MoS_2 a promising candidate for a multitude of potential applications in optoelectronics.[19,31,50,51] The S vacancies of MoS_2 monolayer exhibit high adsorption capabilities toward nonpolar gas molecules of CO_2 and CH_4 gases,[52] making it a good candidate for gas sensors. For FET, MoS_2 is a more appropriate channel material compared to graphene, since MoS_2 is not zero-bandgap and is not easily disturbed by noise signals.[53] Monolayer MoS_2 displays strong photoluminescence,[54] and the perturbations can change its intensity in the local dielectric permittivity of MoS_2 surface after interaction with the target analyte, e.g., DNA, which makes it a perfect material for photoluminescence (PL) biosensors.[55] Meanwhile, the point defects, grain boundaries, and edges of MoS_2 influence their chemical, electrical, and optical properties.[56] In addition, MoS_2 possesses additional electrochemically active sites (such as point defects, grain boundaries, and edges), which enable MoS_2 to improve the intensity of current in the electrochemical sensor. Moreover, MoS_2 displays excellent biocompatibility,[57] e.g., single-stranded DNA can be adsorbed on the basal plane of MoS_2 by van der Waals force,[58] which is beneficial to biosensor fabrication. Nevertheless, several drawbacks of MoS_2 still limit its development and application. High surface energy causes restacking and reduces the amount of electrochemically active sites. Monolayer MoS_2 is not stable in the ambient environment because of its interaction with water and oxygen.[59,60] Poor electrical conductivity and Young's modulus of MoS_2 limit its sensitivity in electro(bio)chemical sensing.[61,62]

The use of individual 2D materials, in particular graphene and TMDs, for chemical sensing has attracted huge attention in the last decade due to their excellent properties. Not surprisingly, some reviews on functionalized graphene for gas sensing,[25] graphene and graphene oxide (GO) for biosensing,[23] and biosensor and gas sensor based on TMDs[22,31,63] have already appeared. However, in view of the availability of different 2D materials and their properties diversity, their combination in hybrid structures can represent a powerful strategy to exploit their mutual advantages. To this end, the same forces which keep together the layers of 2D materials in the bulk crystal, i.e., van der Waals interactions, can be exploited to stack different types of 2D materials together and form heterostructures. The close contact between the materials at the heterojunction causes a synergistic effect which induces new and improved properties compared to those existing in the isolated pristine components.

Here, we review the most enlightening and recent strategies developed with VDWH, primarily incorporating graphene and TMDs, where the 2D materials are employed as functional platforms to detect and quantify gas, biomolecules, and other organic/inorganic molecules. In this review, such sensors are classified based on the detection methods and targeted molecules to provide an easy-to-follow guide for researchers seeking innovative technologies of 2D heterostructures sensing.

2. Van der Waals Heterostructures: Synthetic Strategies and Applications

VDWH can be produced by stacking two or more 2D materials via their vertical superimposition by exploiting weak VDW interactions holding together adjacent 2D layers. The combination of multiple 2D materials might allow overcoming the intrinsic limitations of every single component and can lead to the emergence of novel peculiar properties that are extrinsic to the individual components.

Dean et al. reported the first example of VDWH in 2010.[64] The group fabricated a vertical heterostructure in which exfoliated monolayer graphene was placed on top of the 2D layer of hexagonal boron nitride (h-BN) laying on a SiO_2/Si substrate. The heterostructure was employed as a transistor in which the h-BN layer worked as an interfacial layer between graphene and SiO_2. This transistor exhibited intriguing new characteristics. The measured carrier mobilities of graphene were almost one order of magnitude greater than analog devices on SiO_2, because of the beneficial role of the atomically smooth surface of h-BN, which is almost completely free of dangling bonds and charge traps. Furthermore, the heterostructure presented reduced roughness and intrinsic doping. In later works, other unique properties of graphene/h-BN heterostructures which were never observed before have been revealed. For example, because graphene and h-BN share nearly identical crystal lattices, when they are superimposed, they generate a periodic moiré pattern which gives rise to some quantum effects such as the superlattice Dirac cone,[65] the Hofstadter's butterfly effect,[66] and the appearance of a small bandgap in graphene.[67]

While heterostructures of graphene/h-BN were the first studied, the highest number of publications has been focused on graphene/TMDs heterostructures. Heterostructures of graphene and TMDs have found many applications as FET with high I_{on}/I_{off} ratios,[68–70] memory devices,[73] ultrasensitive and ultrafast photodetectors[71,72] and light-emitting diodes,[73] photovoltaics,[74] and light-harvesting devices. In most cases, graphene finds application as electrodes in the device, while the TMD layer acts as the semiconductor. On the other hand,

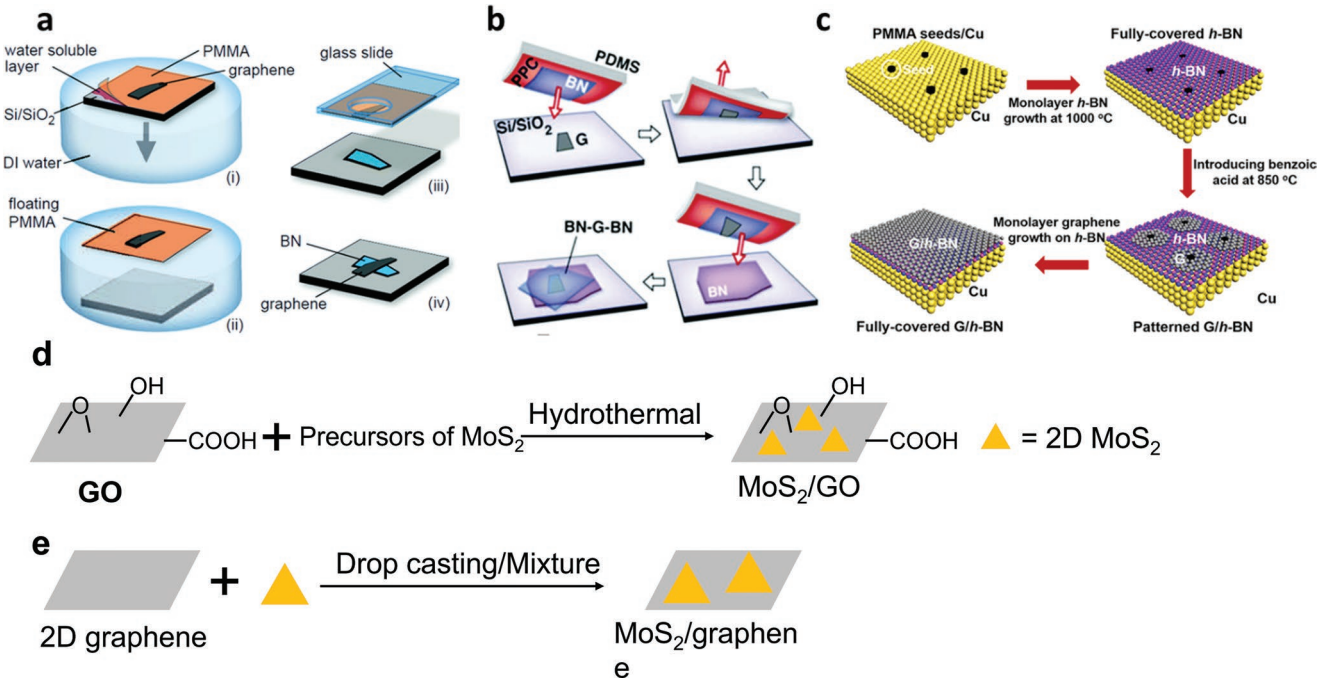

Figure 1. a) Schematic illustration of the "wet" transfer process used to fabricate a graphene/h-BN vertical heterostructure. Adapted with permission.[64] Copyright 2010, Springer Nature. b) Schematic of the fabrication of an h-BN/G/h-BN vertical heterostructure via a dry transfer method. Adapted with permission.[68] Copyright 2013, American Association for the Advancement of Science. c) Scheme of the CVD growth of a graphene/h-BN heterostructure. Adapted with permission.[84] Copyright 2016, American Chemical Society. d) Synthesis of MoS_2/GO by hydrothermal method. e) Synthesis of MoS_2/graphene by drop casting or mixture.

random stacking of graphene and other 2D materials has also found applications in sensing and energy storage (supercapacitors and batteries).[70,75,76]

VDWH can be fabricated by using different techniques in view of the chosen applications. These methods include mechanical transfer, chemical vapor deposition (CVD), and liquid phase assembly. The first method developed by Dean et al. was the mechanical "wet" transfer (**Figure 1**a). One of the two materials was mechanically exfoliated in thin flakes on a rigid substrate, while the second material was exfoliated on top of a poly(methyl methacrylate) (PMMA) membrane. Then, under an optical microscope, the transparent PMMA membrane, supported on a microscope slide, was hung on top of the rigid substrate. With the aid of a micromanipulator, the glass slide was moved to superimpose the two 2D material flakes perfectly, then the PMMA was brought into contact with the rigid substrate, and the two flakes were closely attached by VDW forces. Finally, the PMMA layer was dissolved, yielding the heterostructure. The method has been largely employed to produce different kinds of vertical heterostructures.[68] In addition, by repeating this procedure, complex structures composed of stacks of different materials can be generated.[70,77] Nonetheless, because of the many steps and the use of solvents, contaminants that are hard to be removed can often be found at the interfaces of the 2D materials.[72] For this reason, dry transfer techniques have been developed to avoid the contact of the 2D materials with solvents (Figure 1b).[78,79]

Randomly stacked heterostructures can be produced by mixing different suspensions of single and few-layer 2D materials obtained by liquid-phase exfoliation.[80,81] The formation of stacked heterostructures is driven by the electrostatic and VDW interaction between the two 2D materials flakes. The heterostructures can then be deposited onto arbitrary substrates by means of different techniques (i.e., drop-casting, spin-coating, spray-coating, ink-jet). Mechanical transfer methods produce high-quality heterostructures, mostly suitable for research purposes. Nevertheless, the laborious procedures, the low output volume, and the small size of the obtained heterostructures hinder their applications outside the research area. On the other hand, liquid-phase methods can be easily scalable to produce a high volume of materials; but the often-random nature of the stack jeopardizes their applications.

Large-area vertical heterostructures can be fabricated by employing 2D materials produced by CVD. Spatially extended, individual layers of 2D materials can be grown separately and then stacked together with different transfer methods.[68] Although the transfer of the large CVD layers is simpler than the transfer of mechanically exfoliated flakes which necessitates sub-micrometric precision, the use of solvents and polymers often brings into play the contamination of the surfaces, and the large dimensions of CVD films might result in the formation of wrinkles and cracks.[68] The chemical growth of one kind of 2D material directly on top of another 2D material used as a substrate allows the elimination of the transfer steps with the consequential issues. Numerous direct growth methods that employ different precursors, catalysts, nucleation seeds, temperatures, and techniques (i.e., plasma-enhanced CVD and low-pressure CVD) have been developed to produce a wide variety of VDWHs (Figure 1c).[82–84]

The hydrothermal method[85,86] (Figure 1d) is also a strategy to synthesize VDWHs. Generally, GO was obtained from

graphite by the Hummers method, and then precursors of MoS_2 (such as Na_2MoO_4 and thiourea) were added, the resulting final mixture was transferred to a Teflon-lined autoclave at a high temperature (>200 °C). Some of these works included annealing at 800 °C to remove organic groups or linkers (if there are any). Another more straightforward method is drop coasting 2D-MoS_2 solution on graphene electrode[87] or mix the individual solution of 2D-graphene and MoS_2[88] (Figure 1e).

3. Gas Sensors Based on van der Waals Heterostructures

In the years of IoT, sensors represent fundamental devices capable of collecting information from the external environment and translating them into numerical data. In particular, gas sensors, which can detect the presence and quantify the concentration of a specific gas or vapor in the atmosphere, have become particularly important due to their ability to monitor the air quality we breathe. Gas sensors are largely employed in controlling industrial emissions, environmental pollution monitoring,[89] personal and military safety,[90] medical diagnostics, and atmospheric monitoring in industry and agriculture.[91,92] Most conventional gas sensors nowadays are based on metal oxide semiconductors because of their high sensitivity and low cost; however, they are also characterized by poor selectivity, large energy consumption, high-temperature operation, and limited lifetime.[93] Recently, sensors working at low operating temperatures based on metal oxide semiconductors[94] and conductive polymers[95] have been developed; yet, they feature low sensitivity, slow response/recovery speed, incomplete recovery, and poor stability. In the last years, 2D materials have proven to be promising materials for gas sensing by virtue of their high surface-to-volume ratio, numerous active sites, and high electrical conductivity, which enable the high sensitivity of the sensors.[35,96,97] Moreover, thanks to their extremely low thickness, 2D materials are also transparent and flexible, making them the ideal candidates for wearable devices.[98] Among 2D materials, semiconducting TMDs and phosphorene are particularly appealing because of their adjustable electrical conductivity and sizable bandgaps,[35,99,100] while graphene, with its low electrical noise, makes it possible to detect even extremely small concentrations of gases.[38] The sensing properties of 2D materials, such as sensitivity and selectivity, have already been improved by chemical modification of their surface,[35] or by forming hybrid heterostructures with other (0D, 1D, and 2D) nanomaterials.[101–103] However, the newest frontier consists in combining two or more 2D materials in VDWHs, taking advantage of the synergic interaction between the constituent and the subsequent emergence of new and enhanced properties. In particular, the use of VDWHs may increase gas sensing performances by employing different mechanisms, including the formation of p–n junctions, the photoelectric effect, the improvement of electrical characteristics when interacting with the sensory materials, and the tuning of Schottky contacts. For instance, the use of graphene or other 2D materials as electrodes instead of metals enables flexible sensors which can be potentially used in wearable devices.

It goes in this direction the first example of a gas sensor based on VDWHs, published in 2015 by Cho et al.[99] The group developed a flexible NH_3 and NO_2 chemoresistive sensor based on graphene/MoS_2 heterostructure. First, a few-layers thick MoS_2 flake was mechanically exfoliated and transferred onto a SiO_2/Si substrate, and then a few-layers CVD graphene was patterned by photolithography and transferred on top of the MoS_2 to form interdigitated electrodes (**Figure 2**a). In parallel, a sensor composed of MoS_2 contacted with Au/Ti electrodes was also assembled for comparison. The as-fabricated sensors were exposed to different concentrations of NH_3 and NO_2. Usually, the detected molecules are adsorbed onto the 2D material surface and act as electron donors or acceptors, thereby modifying the charge carrier concentration in the 2D material and, ultimately, its conductivity. Interestingly, while the exposure to the electron-withdrawing NO_2 led to an increase in the resistance in Au/Ti/MoS_2 device, indicating an n-type behavior of the device, the same molecule determined a decrease in the resistance in the graphene/MoS_2 device, as a result of its p-type characteristics. As expected, an opposite behavior was observed for the electron-donating NH_3. In particular, when exposed to 5 ppm of NO_2 and 100 ppm of NH_3, the Au/Ti/MoS_2 device displayed a 31% and −34% response, respectively, while the response to the same gases of the graphene/MoS_2 device was only −6.8% and 3.3% (Figure 2b,c). In both cases, the modulation of resistance due to NH_3 was lower because of the smaller charge transfer of NH_3 compared to NO_2. The lower modulation of the resistance of the device with graphene electrodes was ascribed to the lower contact resistance due to the lowest Schottky barrier between graphene and MoS_2 and the highest resistance of the graphene electrodes. Nonetheless, the graphene/MoS_2 device showed high stability after 5000 bending cycles and long-term stability of 19 months.

The same group[98] also developed another NO_2 and NH_3 flexible sensor with similar geometry but using CVD niobium diselenide ($NbSe_2$) as interdigitated electrodes and tungsten diselenide (WSe_2) as the active sensing material. The device was produced in two steps: first, depositing the patterned transition metal oxide films (WO_3 and Nb_2O_5) in succession with the aid of a shadow mask, and then by selenization of the oxide films using a CVD process. In this case, the height of the Schottky barrier between the two materials was reduced due to the formation of an intermediate transition layer of $Nb_xW_{1-x}S_2$ between the two materials, as was confirmed by XPS, TEM, and EDX analysis (Figure 2d,e). Because of this lowered barrier between the $NbSe_2$ electrode and the WSe_2, its sensitivity toward NO_2 and NH_3 was significantly improved compared to a similar device employing traditional Au electrodes (Figure 2f). In particular, when the $NbSe_2$/WSe_2 was exposed to 1 ppm of NO_2, its current decreased by 27%, compared to the 4% decrease of the Au/WSe_2 device. Similarly, when the devices were exposed to 1 ppm of NH_3, a higher response, yet smaller compared to NO_2, was observed for the $NbSe_2$/WSe_2 device. Furthermore, the VDWH exhibited high selectivity toward NO_2 compared to other gases such as H_2S, N_2O, CO_2, and CO. It showed good retention of the performances after 10 000 bending cycles and after washing in a conventional laundry machine cycle.

VDWHs may also be used to improve the chemical stability and prevent the degradation of the active sensory material.

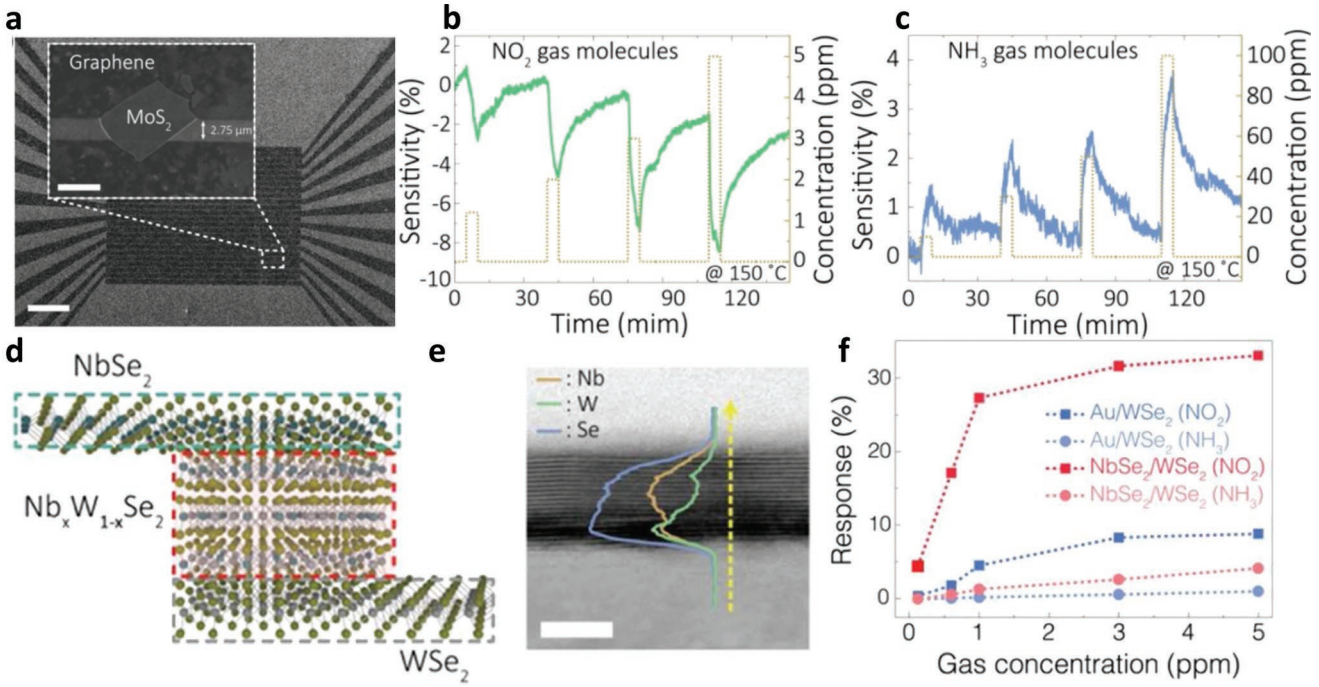

Figure 2. a) SEM image of the MoS_2/graphene sensor (scale bar: 200 μm). The inset image shows the MoS_2 flake bridging two graphene lines (scale bar: 5 μm). b,c) Response of the MoS_2/graphene sensor as a function of time to different concentrations of (b) NO_2 (1–5 ppm) and (c) NH_3 (20–100 ppm). Reproduced with permission.[99] Copyright 2015, American Chemical Society. d) Schematic of the cross-sectional crystal structure of $NbSe_2$–$Nb_xW_{1-x}Se_2$ (transition layer)–WSe_2 heterojunction. e) Cross-sectional X-ray and EDS elemental line scan, indicating the concentration of Nb, W, and S along the *z*-axis coordinate. The scale bar is 5 nm. f) Response of the $NbSe_2/WSe_2$ heterostructure and Au/WSe_2 device to different concentrations of NO_2 and NH_3. Reproduced with permission.[98] Copyright 2016, American Chemical Society.

A good candidate for this purpose is h-BN, a nonconductive and highly stable 2D material,[104] which demonstrated to be an effective barrier against oxidation and degradation when used as an encapsulation layer on top of sensitive 2D materials.[105,106] To this end, Balandin and co-workers[107] produced a heterostructure composed of a MoS_2 flake as an active sensing layer and a larger h-BN flake as a capping protective layer through a dry transfer process. The group demonstrated that the dielectric h-BN capping layer could efficiently protect MoS_2 from degradation in the air while not hampering the sensitivity of the device to different organic vapors. In other examples, h-BN was used as a dielectric layer in FET instead of the conventional SiO_2. The smooth and free of defects surface of h-BN allowed the construction of graphene[108] and MoS_2[109,110] based FET NH_3 and NO_2 sensors combining lower detection limits, higher sensitivity, and faster recovery.

The extreme low thickness of semiconductive 2D materials allows the formation of field-effect vertical tunneling transistors with a very high I_{on}/I_{off} ratio when the 2D material is sandwiched between two graphene layers.[111] With tungsten disulfide (WS_2), Yu and co-workers[112] assembled a field-effect tunneling transistor based on graphene/WS_2/graphene vertical VDWHs and demonstrated that this device could assess the concentration of NO_2 and NH_3 when mixed together (**Figure 3**a). The heterostructure was assembled by stacking single layer graphene (SLG) flake, a 2 nm thick flake of WS_2, and the top SLG with the aid of a micromanipulator. After patterning the flakes into channels with O_2 plasma, Ti/Au metal electrodes were attached to the bottom and top SLG (Figure 3b). WS_2 was chosen because it has the closest electron affinity to those of graphene, thus promising high modulation of the transfer characteristics. In fact, the difference in electron affinity is the most important parameter determining tunneling behavior in tunneling-FET. The electrical characteristics of the device were studied in the absence of sensing gases. The transport curve of the G/WS_2/G device showed n-type transport with high modulation of the tunneling current. In Figure 3c are reported the output curves at different gate voltages (V_G). At V_G = 30 V (red line), the Fermi energies of both top and bottom SLG exceeded the WS_2 tunnel barrier height, and the corresponding output curve was almost linear with Ohmic behavior. On the contrary, at V_G = −30 V (blue line), the Fermi energies of graphene layers were aligned to WS_2 tunnel barrier height, and the output curve showed typical tunneling behavior. The output curve also appeared asymmetric, with the highest variation of the current as a function of V_G for positive V_B because of an intrinsic p-doping of the top graphene layer that led to an inclination of the WS_2 tunnel barrier (insets of Figure 3c). The device was then exposed to 30 ppm of NO_2. The adsorption of the p-doping NO_2 on the device induced rectification behavior, and an increase in the tunneling current, which was a maximum (36% change) for V_G = −30 V and V_b = 0.1 V. Then, the device was exposed to a mixture of NO_2 and NH_3. In Figure 3d is reported the fingerprint map of the response of the device in the off-state (V_G = −30 V and V_b = 0.1) exposed to a mixture of NO_2 and NH_3 with concentration ratios

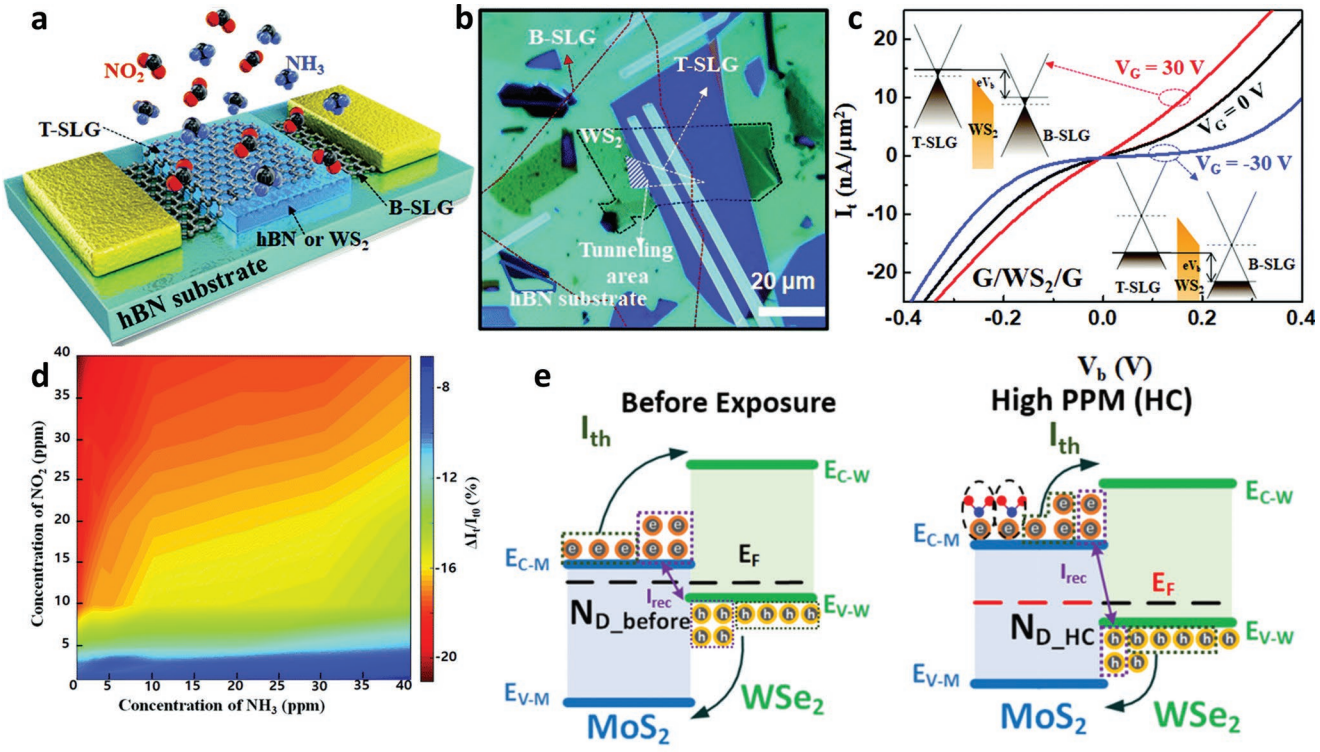

Figure 3. a) Schematic diagram of the NO_2 and NH_3 sensor based on a tunneling G/hBN/G or G/WS_2/G field-effect transistor. b) Optical micrograph of the G/WS_2/G device, c) output curve for the G/WS_2/G FET with different values of $V_G = -30$, 0, and 30 V. Inset: schematics of the energetic diagrams of G/WS_2/G FETs with $V_G = \pm 30$ V and $V_b = 0.1$ V. The dashed lines represent the Fermi energies of top and bottom G. d) Fingerprint mapping of the response ($\Delta I_t/I_{t0}$) of the G/WS_2/G FET as a function of the concentrations of NO_2 and NH_3. Reproduced with permission.[112] Copyright 2017, Royal Society of Chemistry. e) Band energy diagram of a WSe_2/WS_2 p–n junction before and after the exposure to NO_2. Reproduced with permission.[114] Copyright 2021, American Chemical Society.

from 1:40 to 40:1. As expected, the response increased monotonically from 6% to 21% with the increase of the NO_2:NH_3 ratio because of the p-doping and n-doping characteristics of respectively NO_2 and NH_3. Furthermore, the response increased with the concentration of both NO_2 and NH_3 from 1 to 40 ppm when mixed in a 1:1 ratio. The results revealed the higher doping contribution of NO_2 compared to NH_3. In particular, by fitting the data with theoretical models, they found that the adhesion rate of NO_2 molecules' adsorption was almost double that of NH_3 molecules.

Many of the gas sensors based on VDWHs rely on the formation of p–n junctions between the two 2D materials forming the heterostructures. 2D p–n junctions are formed when n-doped and p-doped semiconductor 2D materials are brought into contact. In Figure 3e the band energy diagram of a MoS_2/WS_2 heterostructure before and after the exposure to p-doping NO_2 are reported. Free electrons from the n-doped MoS_2 and holes from the p-doped WS_2 thermally migrate toward the interface and combine together until a charge depletion zone and an electric field which opposes the further diffusion of electrons and holes build up. Looking at the energy bar diagram, when the p- and n-doped 2D material are put in contact, the Fermi levels of the two materials are equilibrated and the valence and the conduction band bend, forming an energy barrier which hinders the passage of holes and electrons. Only by applying an electrical potential higher than this barrier the charge depletion zone is cancelled and current can flow. Thus, p–n junctions work as diodes, allowing current to flow in only one direction, from the p side toward the n side (forward bias). It is worth noting that in 2D p–n junctions the passage of current relies on two mechanisms, which are the thermionic emission and recombination current.[113,114] Both have a linear and exponential correlation to the carrier concentration, applied voltage and energy barrier height. When gas molecules are adsorbed on the heterostructure charge transfer to one or both materials can occur, which causes changes in the carrier concentration and in the Fermi level of each material. These changes in the carrier concentrations lead to changes in the resistance of each material and variation of the energy barrier height, ultimately leading to huge changes in the current flowing through the junction.

The first example of a gas sensor based on a p–n VDWH was published by Zhang and co-workers in 2016.[113] The sensor was based on a heterostructure between few-layered phosphorene (BP) and MoS_2 flakes and employed to sense NO_2. The heterostructure was fabricated on a SiO_2/Si substrate by employing an all-dry transfer method. Finally, two Ti/Au electrodes for each material were then deposited through E-beam lithography. The final device consisted of a BP/MoS_2 p–n junction with two FETs connected in series at the two sides of the junction (**Figure 4**a). The current measured between the BP and MoS_2 electrode showed typical p–n diode behavior, with

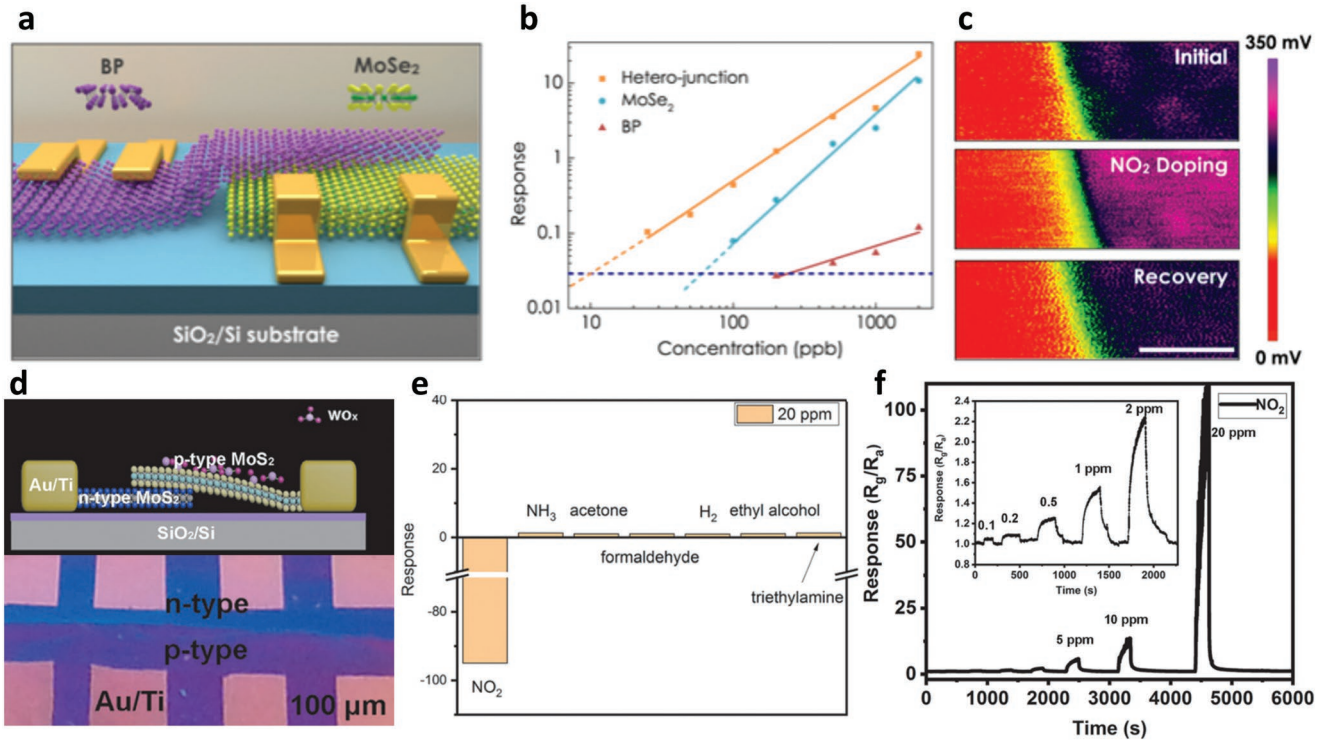

Figure 4. a) Schematic illustration of the BP/MoS_2 heterojunction device. b) Response of all three sensors as a function of gas concentration in logarithm scale. The intersection between each fitting line and the horizontal 3% SNR threshold (blue dashed line) corresponds to the detection limit of each sensor. c) KPFM images of the heterojunction (MoS_2 is on the left and BP on the right) before (top) and after (middle) exposure to NO_2 (500 ppb), and after recovery (bottom). Scale bar is 1 µm. Reproduced with permission.[113] Copyright 2016, IOP Publishing. d) Schematic illustration and image of the p-type/n-type MoS_2 heterostructure. e) Response of the p-type/n-type MoS_2 heterostructure toward 20 ppm of different gases and vapors. f) Response of the p-type/n-type MoS_2 heterostructure as a function of time, when exposed to pulses of NO_2 gas in concentration ranging from 0.1 to 20 ppm. Reproduced with permission.[115] Copyright 2020, John Wiley and Sons.

the highest rectification ratio of 10^3 measured at $V_{gs} = -30$ V. The device was then exposed to different concentrations of NO_2 gas (Figure 4b). The p-type BP FET displayed a weak response to 200 ppb of NO_2, as evidenced by a decrease in resistance of 2.7% due to the boosted hole carrier concentration when the channel is exposed to NO_2. On the contrary, the resistance increased dramatically when n-type MoS_2 was exposed to NO_2, with a response of 28% to 200 ppb of NO_2, as a result of lower electron concentration in the MoS_2 channel and higher Schottky barrier between MoS_2 and electrodes. The response of the BP/MoS_2 heterojunction was found to be even higher, with a 10.5% increase in the resistance when exposed to 25 ppb of NO_2. The detection limit of the heterojunction was six times higher than the one of the MoS_2 FET. Kelvin Probe force microscopy was employed to cast light onto the increased performance of the heterostructure. It revealed the presence of a built-in potential of 150 mV across the heterojunction. Such potential increased to 180 mV upon adsorption of 500 ppb of NO_2, and went back to 150 mV when the gas was removed (Figure 4c). This increase of the built-in potential, together with a higher ratio between holes (from BP) and electrons (from MoS_2), led to a higher energy barrier for electron conduction in MoS_2, which translated to a large increase in the resistance when the heterojunction was exposed to NO_2.

Recently, Zhang and co-workers[115] developed a NO_2 sensor based on a 2D heterojunction between n-type and p-type MoS_2. The monolayer n-type MoS_2 was obtained by conventional CVD process starting from MoO_3 precursor, while the few-layers p-type MoS_2 was obtained by spin-coating W-doped molybdenum acid peroxide sol–gel precursor, followed by sulfurization. The heterostructure was formed by mechanically stacking the few-layers p-type MoS_2 on top of the n-type MoS_2 through a polymethacrylate assisted transfer method (Figure 4d). First, the sensing characteristics of the individual components were evaluated. The sensors were exposed to different gases and vapors to assess their cross-sensitivity. The sensor based on the n-type MoS_2 exhibited the highest sensitivity to triethylamine (TEA) while the p-type MoS_2 device instead showed the highest selectivity toward NO_2, with a very low response to TEA. Finally, the gas sensing characteristics of the MoS_2 p–n junction were evaluated. The sensor exhibited a marked selectivity toward NO_2, with a response to this gas that was at least 50 times superior to all the other interfering gases, including TEA (Figure 4e). In particular, the response to 20 ppm of the MoS_2 p–n junction was 60 times higher compared to the one of p-type MoS_2, and its LOD was just 8 ppb. Response and recovery times toward 5 ppm of NO_2 under UV irradiation were 150 and 30 s, respectively (Figure 4f). Reproducibility was accurate, and long-term stability was acceptable, with a 25% decrease of the response after 6 months. According to the authors, the exposure to TEA, which is an electron donor molecule, produces a small change in the electrical conductivity

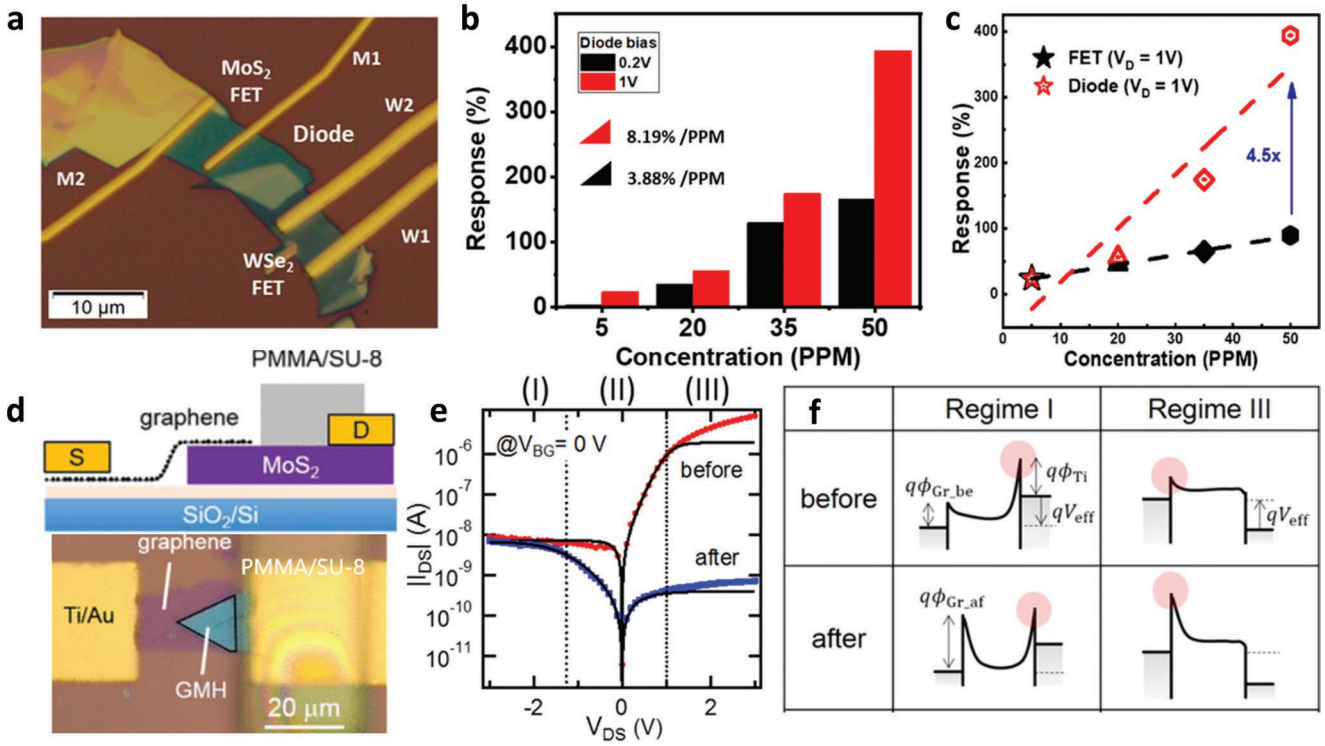

Figure 5. a) Optical image of the p–n diode based on the WSe_2/MoS_2 heterojunction. b) Twofold response of the WSe_2/MoS_2 diode at near zero (0.2 V) and high (1 V) bias to different concentrations of NO_2 ($V_G = -15$ V). c) Response of the WSe_2/MoS_2 diode and MoS_2 FET to different concentrations of NO_2. Reproduced with permission.[114] Copyright 2021, American Chemical Society. d) Schematic illustrations of the cross-section of a G/MoS_2 heterojunction gas sensor(top) and optical image of the sensor (bottom). e) Output curve of the G/MoS_2 sensor before and after the exposure to 1 ppm NO_2 ($V_G = 0$ V) with highlighted regime I (at $V_{DS} = -2$ V) and regime III (at $V_{DS} = 2$ V). Energy band diagram of the G/MoS_2 sensor in the regime I and III before and after NO_2 exposure. In red circles are indicated the bottleneck barriers limiting the drain current. Reproduced with permission.[116] Copyright 2018, American Chemical Society.

of the heterojunction because, on the one hand, decreases the carrier concentration across the p–n junction, thus decreasing its conductivity; on the other hand, it increases the conductivity of the device by decreasing the p–n junction barrier height. On the contrary, the huge decrease in the current of the heterojunction when exposed to NO_2 can be ascribed to an increase in the p–n junction barrier height and a decrease in the carrier concentration across the p–n junction.

An NO_2 and trinitrotoluene (TNT) sensor based on a p–n heterojunction between p-type WSe_2 and n-type MoS_2 was developed by Dhara et al.[114] The heterostructure was fabricated by a PDMS-assisted dry transfer method of the mechanically exfoliated WSe_2 and MoS_2 few-layers flakes on a SiO_2/Si substrate. Cr/Au electrodes were then deposited on top (**Figure 5**a). The device exhibited typical diode characteristics, with a high rectification ratio (7.5×10^4). Then, the device was exposed to NO_2, and its behavior was compared to that of a MoS_2 FET assembled on the same MoS_2 flake. The p–n junction exhibited a twofold response to NO_2 (Figure 5b). At high bias (1 V), a high sensitivity response was observed, which was dominated by the exponential change in the thermionic current due to the increase in the p–n junction barrier height when the device was exposed to NO_2. At near-zero bias (0.2 V), the sensing mechanism was dominated by the carrier concentration change at the interface, which led to a linear change in the interlayer recombination current. Compared to the MoS_2 FET, the p–n junction exhibited a four to six times higher sensitivity over the entire bias range (Figure 5c) and eight times lower detection limit (150 ppb for the p–n junction). The response of the p–n junction was also enhanced using negative gate voltages and thinner MoS_2 flakes. Moreover, the authors found out that the recovery of the sensor was accelerated without the use of the high temperature of UV light by reversing the polarity of the gate for a few seconds after the exposure to NO_2. Finally, the p–n sensor also exhibited a high sensitivity to TNT, with an LOD of just 80 ppb.

Devices based on VDWH of graphene and a TMD can be considered Schottky diodes due to the almost metallic nature of graphene and the semiconductive nature of most TMDs. However, unlike conventional metals, the work function of graphene can be easily modified by interaction with electron-donating or electron-withdrawing gases. This, together with the valence band and conduction band modulation of the TMD, guarantees a high modulation of the Schottky barrier height and thus of the conductivity under exposure to doping gases. Tabata et al.[116] developed a NO_2 sensor based on a graphene/MoS_2 heterojunction. The VDWH consisting of a CVD graphene layer on top of a mechanically exfoliated few-layer MoS_2 flake was assembled through a dry transfer method on a SiO_2/Si substrate. To isolate the response of the heterojunction, all but this were encapsulated with PMMA (Figure 5d). Then, the authors exposed the device to 1 ppm of NO_2. The resistance

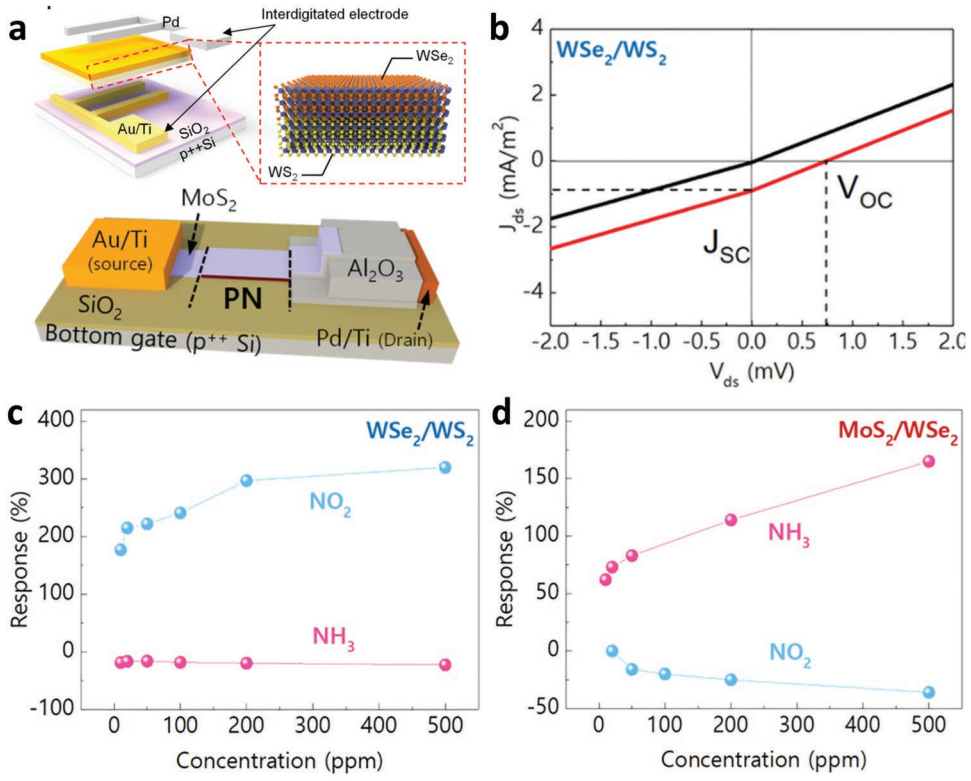

Figure 6. a) Schematic illustrations of the WSe_2/WS_2 (top) and MoS_2/WSe_2 (bottom) gas sensors. b) *I–V* characteristics of WSe_2/WS_2 gas sensor under dark (black line) and light conditions (red), with indicated open-circuit voltage (V_{OC}) and short-circuit current (J_{SC}). c,d) Response of (c) WSe_2/WS_2 and (d) MoS_2/WSe_2 gas sensor to different concentrations of NO_2 and NH_3. Reproduced with permission.[117] Copyright 2020, John Wiley and Sons.

of the device increased, indicating a typical n-type behavior. The response to 1 ppm of NO_2 was greater than 5×10^3 at $V_{DS} = 3$ V. Conversely, the response was two orders of magnitude lower at negative bias and 240 times lower at very positive gate bias ($V_{BG} = 40$ V) (Figure 5e). These results confirmed that the response to NO_2 was due to an increase in the work function of graphene compared to MoS_2, and a consequent increase in the MoS_2/G Schottky barrier height, as illustrated in Figure 5f. The higher response at positive bias could be explained by the lower height of the Schottky barrier at this potential, which guaranteed a higher modulation by the effect of NO_2 (regime III in the figure). At very positive gate bias and negative source–drain bias, the sensor current was limited by the MoS_2/Ti Schottky barrier height and thus mostly independent of the modulation of the MoS_2/G barrier (regime I in the figure).

The p–n junctions can also exhibit a photovoltaic effect, which in principle can be used to assemble self-powered gas sensors. Kim et al.[117] recently succeeded in this intent by assembling two NO_2 and NH_3 sensors based on the VDWHs WSe_2/WS_2 and MoS_2/WSe_2. The first heterostructure, consisting of a vertical heterostructure of trilayer WSe_2 and trilayer WS_2, was synthesized by a one-step CVD process. Then, the photovoltaic device was assembled by transferring the heterostructure on top of a patterned Au/Ti cathode on SiO_2/Si substrate and by finally patterning the Pd anode on top of the heterostructure (**Figure 6**a). The second heterostructure MoS_2/WSe_2 was synthesized by depositing on a SiO_2/Si substrate three-layer WSe_2 followed by monolayer MoS_2 through a self-limiting vacuum-based synthetic process. The final device, comprising the Au/Ti and Pd/Ti electrode, was manufactured through a combination of photolithographic processes (Figure 6a). Both devices exhibited p–n characteristics and photovoltaic effect under white light illumination. At $V_{DS} = 0$, both devices presented no current in the dark, while a photocurrent was observed under light illumination because of the generation of optically excited carriers (Figure 6b). Therefore, the devices were operated at zero bias and under illumination to sense NO_2 and NH_3 gases. The responses of the two devices to different concentrations of these gases are reported in Figure 6c,d. The WSe_2/WS_2 exhibited an increase of photocurrent when exposed to NO_2, with a response of 178% to a gas concentration of 10 ppm, while NO_3 produced a decrease of current with a response of –19% at 10 ppm. On the contrary, the MoS_2/WSe_2 device exhibited a lower and negative response to NO_2 (–15% at 50 ppm) and a higher and positive response to NH_3 (62% at 10 ppm). Response and recovery times were, respectively, 6 and 12 min for the WSe_2/WS_2 device and 3 and 4 min for the MoS_2/WSe_2 device.

One step ahead of diodes based on p–n junctions, there are bipolar junction transistors formed by two consecutive p–n junctions (p–n–p or n–p–n configurations). In 2019 Liu et al.[118] reported the first example of a vertical bipolar junction transistor based on a vertical VDWH of $MoS_2/WSe_2/MoS_2$ with n–p–n configuration and successfully used it to sense NH_3 vapors. The VDWH was formed by vertically stacking through a

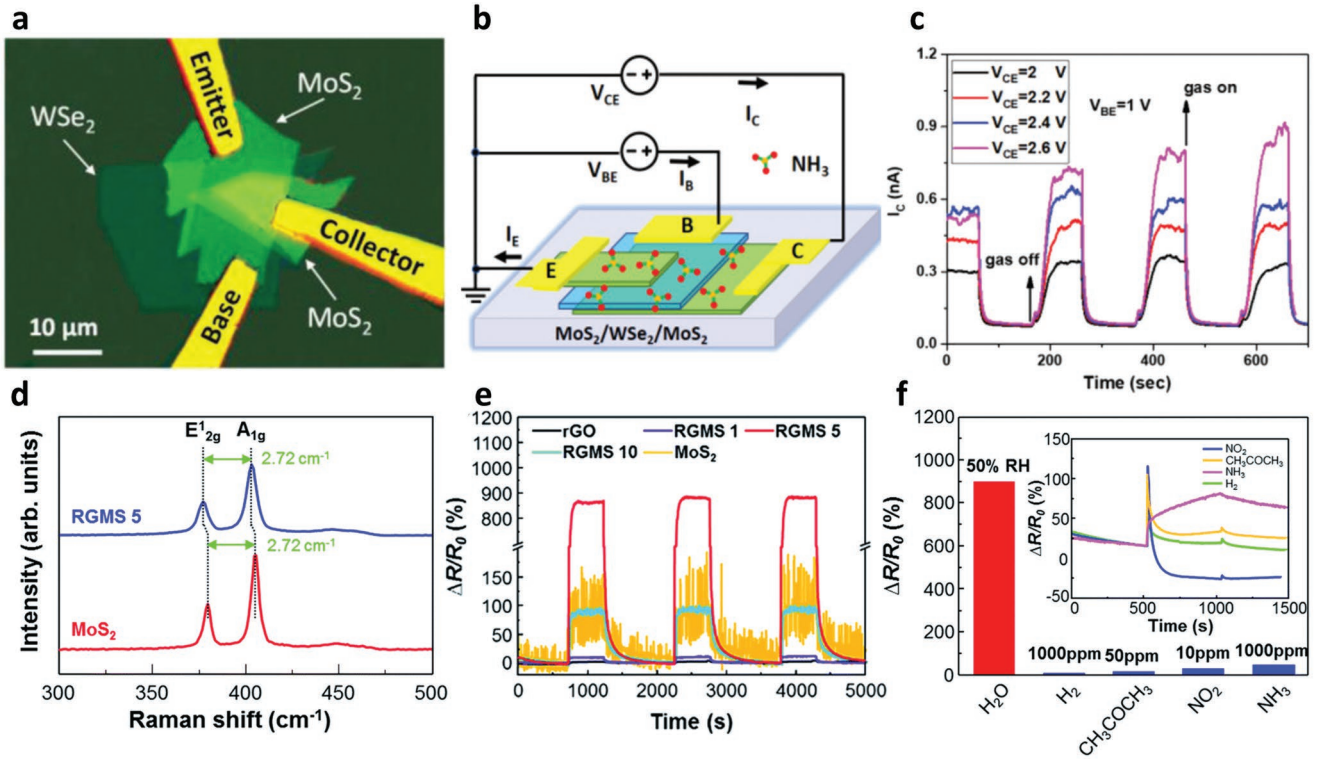

Figure 7. a) Optical microscope image of the bipolar junction transistor based on a vertical VDW heterostructure $MoS_2/WSe_2/MoS_2$. b) Schematic illustration of the gas-sensing experiment in the common-emitter configuration. c) Current output as a function of time of the bipolar junction transistor with sequences of 100 s of NH_3 (50 ppm) and 100 s of air exposure recorded for different values of VCE. Reproduced with permission.[118] Copyrights 2019, Wiley-VCH Verlag GmbH & Co. KGaA. d) MoS_2 Raman spectra of pure MoS_2 and of the hybrid rGO/MoS_2. e) Response as a function of time to pulses of humid air (50% RH) of rGO, MoS_2, and the hybrid of the two (with rGO/MoS_2 ratios 1:1, 1:5, 1:10). f) Response to humidity and various types of gases (HO_2, CH_3COCH_3, NO_2, and NH_3) of the hybrid rGO/MoS_2 (1:5 ratio). Reproduced with permission.[120] Copyright 2018, Royal Society of Chemistry.

dry transfer method mechanically exfoliated flakes of few-layers MoS_2 and WSe_2 on a Si/SiO_2 substrate (**Figure 7**a). First, the bipolar junction transistor characteristics were investigated. The device showed a common-emitter current gain of 12 and a common-base current gain of 0.97. Finally, the device was tested as an NH_3 sensor in the common-emitter configuration by measuring the variations of the collector current (Figure 7b). The device displayed a 12-fold increase in the current when exposed to 50 ppm of NH_3 (Figure 7c). The response and recovery times were 9 and 17 s, respectively, and the power dissipation was only 2 nW. The same strategy was used to assemble a $WSe_2/MoS_2/WSe_2$ p–n–p bipolar junction transistor with high selectivity and sensitivity toward NO_2 (18-fold current decrease at 50 ppm), fast response (26 s) and recovery (14 s). The vast majority of VDWHs are produced either by stacking mechanically exfoliated flakes or by CVD methods. The first is a feasible technique for prototyping and research yet not for industrial scale-up, while the latter has more industrial potential yet is still too expensive. Liquid phase exfoliation allows to produce 2D materials in high yield and at a lower cost. For instance, nanohybrids of 2D materials in which the flakes are held together by VDW forces can be obtained by simultaneous liquid-phase exfoliation of the two bulk materials. Jha and Guha produced a coexfoliated nanohybrid of WS_2 and WSe_2 and used it to sense humidity.[119] The heterostructure was produced by simultaneously exfoliating WS_2 and WSe_2 bulk powder in a mixture of ethanol and water with the aid of ultrasonication. High-resolution TEM and EDX confirmed the formation of a WS_2/WSe_2 heterostructure in the hybrid. The coupling between the two materials was further confirmed by the appearance of a new vibrational mode at 317 cm^{-1} in the Raman spectrum due to interlayer coupling in the hybrid. The humidity sensor device was then assembled by drop-casting the nanohybrid on a SiO_2/Si substrate with gold interdigitated electrodes. The device exhibited an increase in the current when exposed to humidity, which varied between 15 times at 40% relative humidity (RH) and 57 times at 80% RH. The device also showed a hysteresis lower than 3% and responses and recovery times of 40 and 65 s, respectively. The response of the hybrid device was studied as a function of the ratio between the two components in the hybrid and also compared to one of the single exfoliated components. The response was highest in the devices utilizing a 1:1 proportion of the two 2D materials and was 40% lower in the device with the single components. The better performances of the hybrid were explained by the modulation of the surface barrier potential, which promoted the adsorption of water molecules at the interface and enhanced the charge transduction. Furthermore, the formation of p–n junctions produced an interface resistance that was modulated by the presence of water. Jang and co-workers prepared a VDW nanohybrid of reduced graphene

oxide (rGO) and MoS_2 and employed it to sense humidity.[120] The hybrid was produced by homogenizing a suspension of the two materials in water with the aid of ultrasonication. Different ratios of the two materials were used, although the best results in humidity sensing were obtained when using a molar ratio between MoS_2 and rGO corresponding to 5. The formation of a nanohybrid in which the two 2D materials were interacting by VDW forces was confirmed by TEM, Raman spectroscopy, XPS, and UPS analyses. In particular, TEM showed the intimate coexistence of the two 2D materials, while a blue shift of the peaks in the MoS_2 Raman spectrum (Figure 7d) and in the XPS survey spectrum of the hybrid confirmed the binding of MoS_2 to rGO and the electron transfer from the n-type MoS_2 to p-type rGO. UPS exhibited the decrease and increase of the work function of rGO and MoS_2, respectively, thus confirming the n-type behavior of MoS_2 and p-type behavior of rGO. The hybrid material was deposited by drop-casting on SiO_2/Si and flexible PET substrates with interdigitated Pt/Ti electrodes to produce the sensing device. Figure 7e portrays the response of the devices based on rGO, MoS_2, and the hybrid to pulses of humid air. In all cases, the resistance increased with humidity; however, the sensitivities were strongly different: the responses to pulses of humid air were 4.1%, 70.7%, and 872% for rGO, MoS_2, and the hybrid, respectively. Furthermore, the signal-to-noise ratio was dramatically improved in the hybrid compared to the pure MoS_2 device. In fact, due to its high base resistance, the device with MoS_2 showed a very high noise. In the range 5% to 85% RH, the response of the MoS_2/rGO device was equal to 2494%. Furthermore, the hybrid device showed high selectivity to humidity (Figure 7f), fast response (6.3 s) and recovery (30.8 s), high repeatability, long-term stability, and flexibility (of the device on the PET substrate). According to the authors, the better performances of the hybrid were due to an increase of the active sites for the adsorption of water in the hybrid, as well as to the formation of p–n junctions at the interface between the two materials. In particular, the water molecules, acting as electron acceptors, increased the p–n potential barrier height, thus leading to a dramatic increase in the resistance.

In Table 1 we summarized all the sensors treated in this section of the review, with indicated the synthetic methods utilized as well as the principal figures of merit of each sensor (sensitivity, limit of detection, response, and recovery times).

By and large, in the first part of this review, we have provided critical insight into the latest development in the application of VDWHs as gas sensors. We endeavored to show that some intrinsic properties of VDWHs, such as the formation of p–n junctions or Schottky junctions, are extremely favorable to gas sensing applications since the modulation of their energy barrier height when the heterostructures interact with electron-donating or electron-withdrawing gases provides a huge modulation of the device current, and ultimately a huge sensitivity. Furthermore, we emphasized the high versatility of these heterostructures; indeed, the selection of different materials with different work functions and bandgaps among the vast library of 2D materials, makes it possible to target selectively specific gases. For the same reason, a sensor's sensing properties and selectivity can change dramatically by simply swapping the top material, in contact with the analyte, with the bottom one. Flexible and self-powered photovoltaic sensors pave the way for wearable, autonomous devices. Yet, further research is needed, especially toward the sensing of volatile organic compounds and CO_2. Recent computational works on VDWHs of borophene/MoS_2[121] and nitrogenated holey graphene/graphdiyne[122] forecast a high sensitivity of these heterostructures toward toluene, acetylene, and formaldehyde, although the synthesis of these new 2D materials remains highly challenging. The ability of the sensors to differentiate the gases within a mixture must be improved, and the influence of the environment and humidity on the performance of the sensor must be better understood. The long-term stability of the sensors is a crucial parameter for the industrial scale-up, and yet it is too seldom assessed. In addition, to make VDWHs appealing to enter the market, important drawbacks such as their high cost and cumbersome production processes still need to be addressed.

4. Electrochemical Sensors and Biosensors Based on 2D Material Heterostructures

In this section, we define an electrochemical sensor to detect specific substances nonpossessing obvious bioactivity by converting chemical data into electronic signals. A biosensor is defined as a device that contains biologically active ingredients (such as protein and enzyme) or detects biomolecules (such as DNA, ascorbic acid, and dopamine). Herein, we focus on the most recent developments in the functionalization of electrochemical sensors and biosensors based on VDWHs, which exploit the combination of 2D materials to improve the sensing performance of target molecules due to their synergistic effects. These synergistic effects include better dispersion of MoS_2, enhanced stiffness while lower yield strain due to the lattice mismatch between MoS_2 and graphene, and lateral buckling of graphene,[123] fast electron transport network with highly active sites,[124] and higher conductivity of the hybrid in general.[125] In particular, significant advances were recently achieved in chemical sensors and biosensors exhibiting i) high selectivity, ii) low detection limits, iii) good stability and reproducibility, iv) rapid response, and v) a wide linear range. Herein, we highlight the most enlightening results to offer the reader an overview of 2D materials for electrochemical sensors and biosensors.

4.1. Electrochemical Sensors

The excellent properties of graphene and related materials, such as the high specific surface area and the outstanding conductivity,[126–128] are also beneficial for application as electrochemical (bio)sensors. In addition, TMDs, especially MoS_2, possess additional electrochemically active sites. Therefore, the hybridization of graphene-based materials with TMDs enables them to combine their advantages and improve their electrochemical performance. The graphene/MoS_2 heterostructure characteristics are strongly dependent on their structures and state, such as layer numbers and oxidation degrees. Among various analytes, H_2O_2 is essential for clinical research because it is a key intermediate in biological and environmental systems. For example, cancer and neurodegenerative diseases

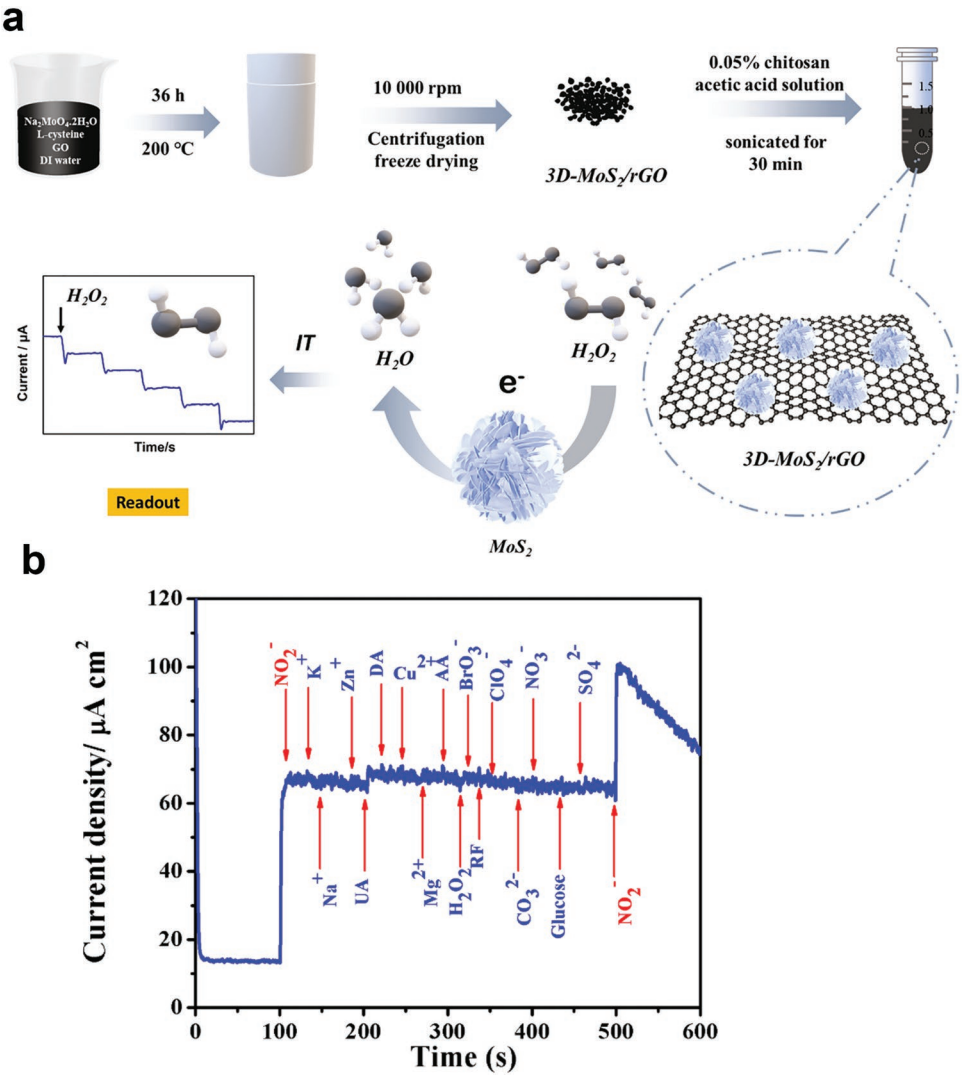

Figure 8. a) Fabrication and detection process of the electrochemical sensor. Reproduced with permission.[129] Copyright 2021, Elsevier B.V. b) Current density–time curve recorded on the rGO–MoS_2–PEDOT/GCE 0.1 M PBS (pH = 4) upon successive addition of 10 μM nitrite and various common anionic and catanionic interference (100 μM) and physiological active species (200 μM) at the applied potential of 0.95 V versus SCE. Reproduced with permission.[133] Copyright 2019, Elsevier B.V.

can lead to an increase in the level of intracellular H_2O_2. The improvement of electrode sensitivity and detection limit toward H_2O_2 via modified glassy carbon electrode (GCE) with a 3D structure of MoS_2/rGO was developed by Yang et al.[129] They showed that rGO acts as a supporting platform and generates the porous structure, which significantly improved the surface area of the MoS_2/rGO, resulting in higher sensitivity. The fabrication and detection process of the MoS_2/rGO sensor is illustrated in **Figure 8**a. An LOD of 0.19 μM and linear range of 2 μM to 23.18 mM were achieved for H_2O_2. Moreover, the repeatability and stability of the MoS_2/rGO electrochemical sensor were demonstrated by the low relative standard deviation (RSD) of 4.98% and the 92.31% response of the original current after 15 days. An amperometric sensor for detecting H_2O_2 was fabricated by using flower-like MoS_2 nanostructure grown on graphene and multiwalled carbon nanotubes (MWCNTs).[130] MWCNTs induced MoS_2 to adopt a flower-like morphology and served as conducting wires connecting all MoS_2 resulting in a good conductivity. The resulting sensor displayed rapid responses toward H_2O_2 detection with a concentration range of 5–145 μM with an LOD of 0.83 μM.

The ion nitrite (NO_2^-) is a common inorganic contaminant, and it is hazardous to both the environment and human health. Therefore, hybrid graphene/MoS_2 has been integrated into sensing devices to detect NO_2^- with enhanced sensitivity. Hu et al. reported an rGO/MoS_2 heterostructure modified GCE to detect NO_2^- by cyclic voltammetry (CV) and single-potential amperometry methods.[131] They observed a linear range of 0.2–4800 μM, LOD of 0.17 μM, and high sensitivity of 0.46 μA μM^{-1} cm^{-2} at 0.8 V versus Ag/AgCl. The good sensitivity is attributed to the synergistic effect of rGO and MoS_2 and the unique nanoarchitecture of rGO–MoS_2, increasing the surface contact area with the analytes and facilitating the electrochemical reactions. The selectivity of the rGO–MoS_2 sensor

toward nitrite was demonstrated by the incorporation of Na_2SO_4, KCl, $NaNO_3$, Na_2CO_3, glucose, and alcohol into the solution. Only the addition of nitrite could increase the corresponding current, while no changes in the electrical characteristics have been observed upon the addition of other substances. A similar result was obtained by integrating rose-like Au nanoparticles and MoS_2 nanoflower/graphene-modified electrochemical sensor.[132] The Au nanoparticles enlarged the surface area of gold nanoparticle (AuNP)/MoS_2/Gr, leading to more exposed electroactive S–Mo–S edges, ultimately improving the catalytic activity for $NaNO_2$. Madhuvilakku et al. achieved a lower LOD of ≈0.059 µM (S/N = 3) and a wide linear range (0.001–1 mM) for detecting NO_2^- by a combination of poly(3,4-ethylene dioxythiophene) (PEDOT) and rGO/MoS_2.[133] In the work, the PEDOT nanoparticles displayed an average size of 100–120 nm and were homogeneously distributed on the surface of rGO/MoS_2 nanosheets, which increased the accessible surface area by inhibiting aggregation of rGO/MoS_2 thereby facilitating the diffusion of NO_2^- at the surface and in bulk. The current density regarding NO_2^- oxidation of rGO/MoS_2/PEDOT-modified GCE amounts to 1.7- and 15-fold when compared to rGO/MoS_2/GCE and bare GCE, respectively. The improved electrocatalytic performance can be ascribed to rGO/MoS_2 synergistic effect, as well as the unique morphology with a high surface area and superior electrical conductivity. The authors also used the amperometric method to explore the selectivity of the rGO/MoS_2/PEDOT/GCE sensor toward nitrite in the presence of various ions and physiological interference, as shown in Figure 8b.

Pesticides not only protect crops but also threaten food safety, which is important for human health since most pesticides are toxic. MoS_2/graphene nanocomposite-based sensors were developed to detect methyl parathion, an organophosphorus pesticide derivative.[85] The authors utilized the hydrothermal process to obtain MoS_2/graphene nanocomposite, which was further used to modify GCE. Enhanced electrocatalytic ability toward methyl parathion was observed at –0.60 V (vs Ag/AgCl), and the linear range is from 10 nM to 1.9 mM, with an LOD of 3.2 nM (S/N = 3). The authors attributed the good performance of the 3D network of MoS_2/graphene to the largely exposed electrochemically active area and the synergistic effect of graphene and MoS_2. Furthermore, the determination of methyl parathion in spiked samples of homogenized apple, kiwi, tomato, and cabbage was conducted with good recoveries.

MoS_2/graphene-based sensors can also be used for the detection of common drugs and precursors. A eugenol sensor has been reported by Feng et al. based on poly(diallyl dimethylammonium chloride) (PDDA)-functionalized graphene–MoS_2 nanoflower materials (PDDA/Gr/MoS_2) with AuNPs.[86] The proposed scheme for the preparation of PDDA/G/MoS_2 and Au is shown in **Figure 9**a. The enhanced electrochemical signal

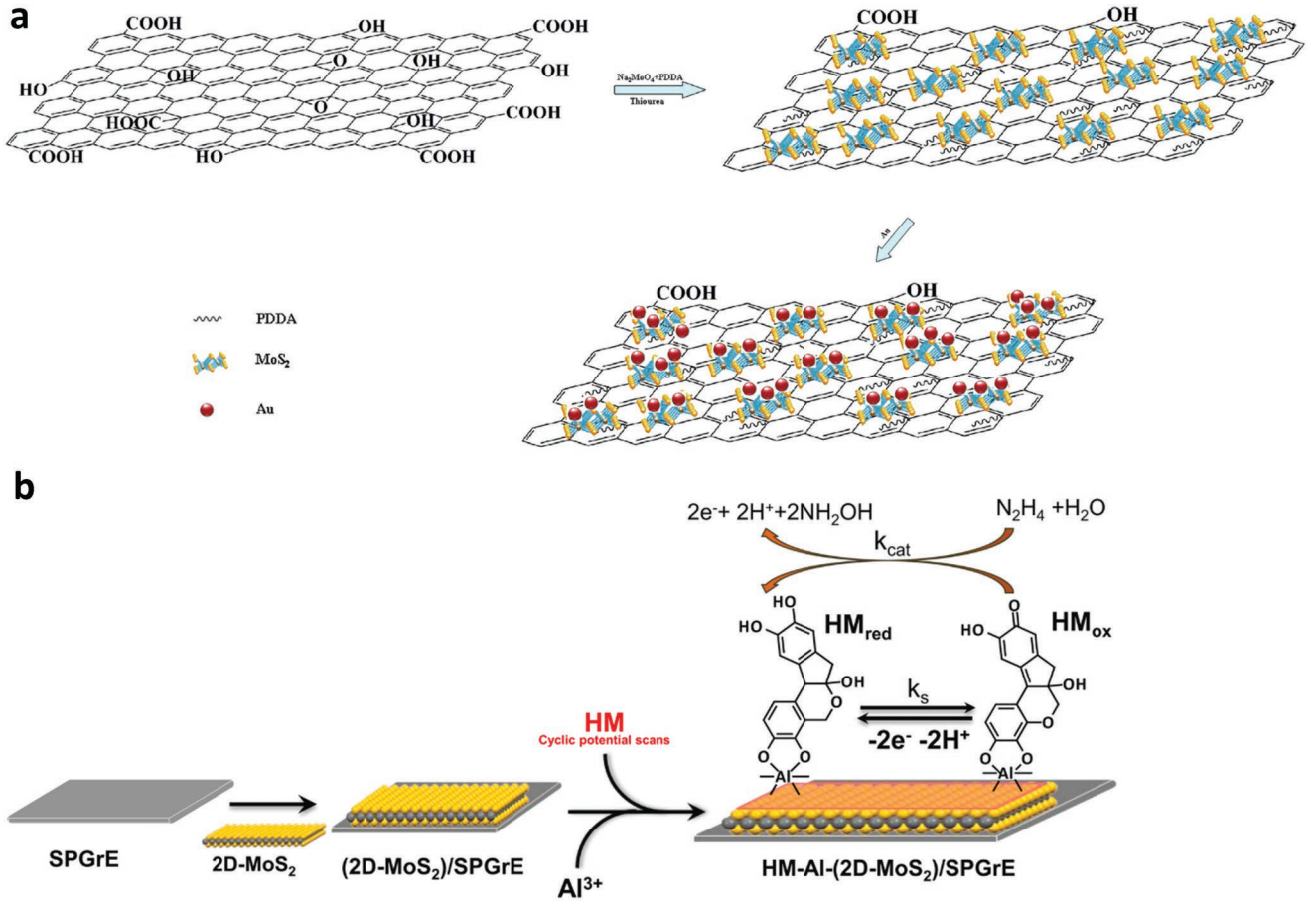

Figure 9. a) The proposed scheme of the preparation of PDDA-G-MoS_2 and Au. Reproduced with permission.[86] Copyright 2013, Elsevier B.V. b) Sensor development for hydrazine detection. Reproduced with permission.[87] Copyright 2021, Elsevier B.V.

of eugenol was achieved by the large specific surface area of PDDA–G–MoS_2 and high conductivity AuNPs. The authors reached a linear range of 0.1 to 440 μmol L^{-1} with an LOD of 0.036 μM (S/N = 3) in 0.10 mol L^{-1} NaAc–HAc buffer solution (pH = 5.50). For the determination of eugenol in perfume and pharmaceutical capsules, the as-prepared sensor displayed the recoveries of 99.8–102.1%, and the RSDs were <3%. Layered MoS_2/graphene composites were previously used for sensitive detecting acetaminophen.[134] The resulting electrochemical sensor showed excellent electrocatalytic activity toward acetaminophen in the linear range of 0.1–100 μmol L^{-1} and LOD of 0.02 μM (S/N = 3). Demir et al. described a paracetamol (acetaminophen, Ac) sensor based on the screen-printed electrode (SPE) modified by MoS_2 with TiO_2 forming a heterostructure with rGO (MoS_2–TiO_2/rGO).[135] They optimized the ratio of rGO:MoS_2–TiO_2, the amount of MoS_2–TiO_2/rGO composite on the SPE, and the pH of the electrolyte to achieve good performance for Ac oxidation based on the synergetic effect and increased surface area of MoS2–TiO_2/rGO. Finally, a linear range between 0.1 and 125 μM with a sensitivity of 0.4425 μA μM^{-1} cm^{-2} and LOD of 0.046 μM were achieved. Acceptable recovery values in the range of 101.15% and 102.69% were displayed to determine Ac in the human urine sample and commercial drug sample containing Ac. Screen-printed graphene electrodes (SPGrEs) modified by MoS_2 and hematein (HM) were designed to detect hydrazine (a precursor for pharmaceuticals).[87] MoS_2 and HM formed a ternary complex with Al^{3+} salts as mordant. The procedure of modified commercial SPGrEs procedure is described in Figure 9b. Owing to the quinone/hydroquinone moieties of hematein, the resulting HM-Al^{3+}-(2D-MoS_2)/SPGrEs sensor displays enhanced electrocatalytic activity toward hydrazine oxidation. In addition, 2D-MoS_2 nanosheets strengthen the ability of electron donor/acceptor of hematein, leading to a high electrocatalytic kinetic constant of $(8.1 \pm 0.1) \times 10^4$ M^{-1} s^{-1}. The heterogeneous charge transfer constant (ks) reached 105 ± 2 s^{-1}, suggesting a fast charge transfer kinetic between HM and the electrode surface. A linear range of hydrazine concentration between 3.81 and 400 μM with an LOD of 1.05 μM was reported by the HM-Al^{3+}-(2D-MoS_2)/SPGrEs sensor.

An electronic tongue (e-tongue) based on MoS_2 and GO was reported for detecting antibiotics, being a major breakthrough for human health and also highly relevant to avoid the emergence of antibiotic-resistant bacteria due to abuse and inappropriate disposal.[136] The authors modified gold interdigitated electrodes (IDEs) by MoS_2 and GO with drop-casting. The modified electrode with MoS_2/GO possessed higher capacitance than the modified MoS_2 or GO electrodes. The latter can be ascribed to a higher concentration of available charge carriers and the larger surface area created by prohibiting the restacking and the synergy of MoS_2 and GO. Four antibiotics, cloxacillin benzathine (CB), erythromycin (Ery), streptomycin sulfate (SS), and tetracycline hydrochloride (TH), were detected in this work with concentrations between 0.5 and 5.0 nmol L^{-1}. The as-prepared e-tongue could distinguish the real samples (river water and human urine) at a nanomolar level.

We summarized all the electrochemical sensors discussed in this section of the review in Table 2, with indicated the synthetic methods utilized as well as the principal figures of merit of each sensor (sensing platform, synthesis method, sensitivity, selectivity, response times, LOD).

4.2. Electrochemical Biosensors

Graphene/MoS_2 materials, in view of their good biocompatibility, have attracted wide interest in exploring their functionalization with biomolecules such as nucleic acid aptamers, enzymes, or antibodies acting as a receptor to detect target analytes. Among various biosensors, electrochemical biosensors are easy-to-use analytical techniques and allow the detection of different analytes with fast response, precise and selective monitoring, low cost, and high sensitivity. Based on graphene and MoS_2, electrochemical biosensors can be achieved using different strategies, such as in combination with a multitude of biomolecules and metal nanoparticles. Thus, various proteins have been used for biosensing. Hemoglobin (Hb) with flower-like MoS_2-modified GO nanocomposite has been developed to fabricate mediator-free biosensors for detecting H_2O_2.[137] The MoS_2/rGO nanocomposite was prepared by hydrothermal method and then mixed with the Hb solution to modify the GCE since the interspaces of 3D MoS_2/rGO nanostructure are favorable for immobilizing Hb, which generally displays electrocatalytic activity toward H_2O_2. The as-prepared biosensor exhibited a linear range between 0.1 and 250 μM with a low LOD of 25 nM. Electron transfer between Hb and GCE was improved in Nafion/Hb/MoS_2–rGO/GCE compared to Nafion/Hb/GC, Nafion/Hb/MoS_2/GCE, and Nafion/Hb/rGO/GCE, due to its unique morphology (flower-like MoS_2 on the graphene substrate) and property of the MoS_2–rGO. In 2017, Yoon et al. reported an H_2O_2 electrochemical biosensor based on MoS_2 nanoparticles encapsulated with graphene oxide (GO/MoS_2).[138] In this work, myoglobin (Mb) was selected as the biomolecular element due to its electrochemically active iron ion centre, which can be used to detect H_2O_2 by electrochemical reduction.[139,140] GO/MoS_2 was bonded on a gold electrode with a chemical linker, and then Mb was further immobilized on the GO/MoS_2 layer, as shown in **Figure 10**a. The resulting modified electrode biosensors demonstrated a low detection limit for H_2O_2 (20 nM) and enhanced electrochemical amperometric response than that for Mb without GO/MoS_2, and good selective detection of H_2O_2 in the presence of L-ascorbic acid (AA), $NaNO_2$, and $NaHCO_3$. The authors declared that the good performance may be due to the improved electron-transfer reaction and larger surface area for Mb immobilization induced by GO/MoS_2. Moreover, its reproducibility and stability were up to 9 days at room temperature. The same group used a similar MoS_2/GO/Mb modified gold electrode for detecting nitric oxide (NO) with a detection limit of 3.6 nM.[141] Zhang et al. also developed a biosensor based on layered MoS_2/graphene composites with Mb.[142] First, the electrodes were modified by layered MoS_2/graphene composites, which Mb and Nafion further decorated to generate a stable film. The resulting biosensor demonstrated a linear range of 6.25–225 mM with LOD of 1.25 mM for H_2O_2, and 1.25–12.5 mM with a detection limit of 0.125 mM for $NaNO_2$.

Immobilization of antibodies is a common strategy for biosensors to realize specific detection. An electrochemical

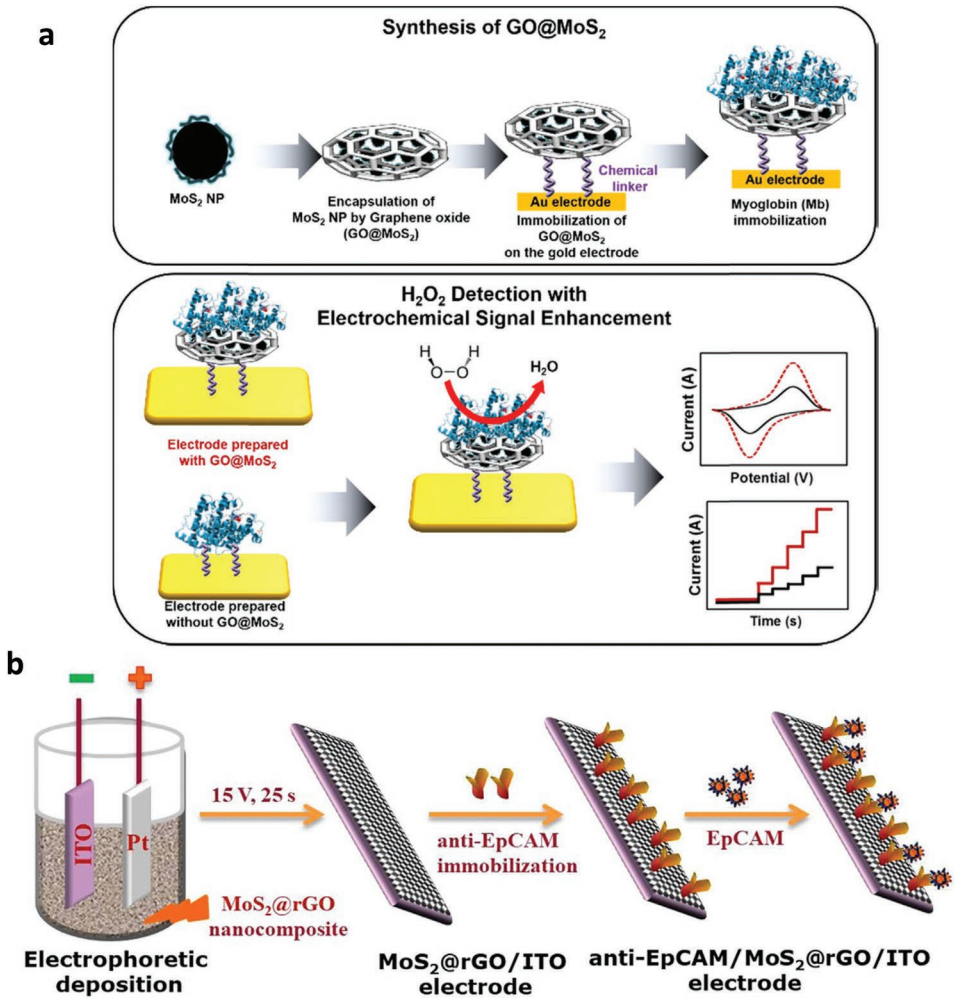

Figure 10. a) Schematic of GO@MoS_2 preparation for the fabrication of electrochemical biosensors composed of Mb and of GO@MoS_2 with electrochemical enhancement for H_2O_2 detection. Reproduced with permission.[138] Copyright 2016, Elsevier B.V. b) Schematic description for the fabrication of rGO@MoS_2/ITO-based biosensor. Reproduced with permission.[143] Copyright 2020, Elsevier B.V.

biosensor was reported by Jalil et al. based on MoS_2-grafted rGO (MoS_2/rGO).[143] It is worth noting that biomolecule L-cysteine (L-cys) was used to reduce GO and bring multifunctional groups for MoS_2/rGO.[144,145] Then, the resulting MoS_2/rGO was modified indium tin oxide (ITO) electrode by electrophoretic deposition and was further covalently immobilized with epithelial cell adhesion molecule antibodies (anti-EpCAM) for specific detecting EpCAM. A schematic description for the fabrication of rGO/MoS_2/ITO-based biosensor is displayed in Figure 10b. The anodic peak current displayed a linear decrease in the EpCAM concentration range of 0.001–20 ng mL^{-1} with LOD of 44.22 fg mL^{-1} (S/N = 3). The authors declared that the efficient immobilization of EpCAM antibodies on the MoS_2/rGO surface led to a good analytical performance with high selectivity, reproducibility, and stability. In this work, rGO is an effective electron promoter, and MoS_2 improves the anti-EpCAM loading, which results in higher interaction between EpCAM antigen and antibodies. Additionally, the anti-EpCAM/MoS_2/rGO/ITO electrode was applied to determine EpCAM antigen in spiked samples, human saliva, serum, and urine, with the recoveries of 91.2%, 95.8%, and 96.2%, respectively.

Enzymes are another biomolecular element for electrochemical biosensors due to their highly specific affinity to the target analyte, and layered 3D structures formed by 2D materials can maintain the stability activity of enzymes. Jeong et al. reported high-performance glucose biosensors based on 3D MoS_2/graphene aerogels (MGAs) by the one-pot hydrothermal method.[146] The resulting 3D MGA-modified GCE with glucose oxidase (GOx) for glucose biosensor demonstrated a fast response (≈4 s), a good linear detection range (2 to 20 mM), high sensitivity (3.36 μA mM), and a low LOD (0.29 mM). Moreover, 3D MGA displayed a better electrochemical performance than the corresponding 2D MoS_2/rGO due to the 3D porous structure of MGA facilitating efficient and rapid pathways for ions and electrons and large surface areas for enzyme immobilization. The selective detection of glucose among ascorbic acid, uric acid, and dopamine is good at an operating potential of –0.45 V.

Freestanding graphene paper (GP) supported MoS_2 nanocrystals monolayer with deposited Cu sub-micrometer buds for biosensing lactate, and glucose in sweat was developed to overcome the limited charge-electron transfer in the enzymatic

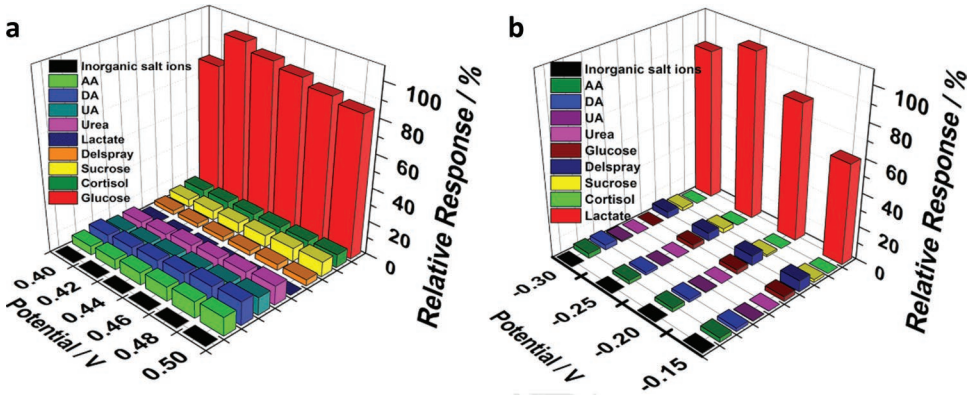

Figure 11. Influence of interferences on the response of a) 5 μM glucose and b) 40 μM lactate. Reproduced with permission.[147] Copyright 2017, Elsevier Inc.

reaction.[147] The authors carried out the amperometric *i–t* method to quantify with a linear range of 5–1775 μM for glucose and 0.01–18.4 mM for lactate. The good performance is ascribed to the high specific surface area of MoS_2 with the closely packed form, which can work as conductive centers to enhance the electron transfer across Cu sub-micrometer-buds and graphene paper, which improves the electron transfer between the redox centre of the enzyme and the electrode. Moreover, the resulting biosensor showed good selectivity for both glucose and lactate, as shown in **Figure 11**. Another electrochemical biosensor based on MoS_2/rGO and Cu_xS ($x = 1$ or 2) was reported by Xu et al.[148] The Cu_xS was well dispersed in the 3D wrinkled porous MoS_2/rGO without evident aggregation, exposing more active sites for catalysis and improving the catalysis. In addition, more active defects on MoS_2 could be led by the heteroatom Cu.[149,150] Therefore, the as-obtained biosensor illustrated a wide linear range from 2 to 6330 μM with an LOD of 0.6 μM. Furthermore, the authors used the Cu_xS/MoS_2/rGO-modified electrode to analyze glucose in human serum samples, and recoveries between 97.2% and 101.2% were observed.

Aptamers are synthetic single-stranded nucleic acids and are popular in biosensors due to their good thermal and chemical stability, low cost, easier synthesis, and high affinity to the target analyte.[151,152] Meanwhile, AuNPs with good biocompatibility[153] can be used to immobilize biomolecular via Au—S bonds. Therefore, based on aflatoxin B_1 (AFB_1) aptamers and AuNPs with rGO/MoS_2/polyaniline nanocomposites, Geleta et al. reported an electrochemical aptasensor for the detection of AFB_1.[154] MoS_2/rGO was first synthesized by hydrothermal method, and then treatment with aniline and ammonium peroxydisulfate yielded MoS_2/rGO/polyaniline hybrids. The polyaniline nanoparticles were evenly distributed on rGO/MoS_2 surface. Finally, the MoS_2/RGO/polyaniline was decorated with AuNPs to generate MoS_2/rGO/polyaniline/AuNPs hybrids. The mechanism of this biosensor relies on the change in conformation of the immobilized aptamer upon binding of AFB_1, with the resulting AFB_1-aptamer pairs inhibiting the electron exchange of $[Fe(CN)_6]^{3-/4-}$, thereby leading to a lower peak current in the differential pulse voltammetry (DPV) measurement. The as-developed aptasensor displayed a wide linear range between 0.01 and 1.0 fg mL^{-1}, low LOD of 0.002 fg mL^{-1} due to large surface areas and good conductivity. Moreover, the high selectivity for detecting AFB_1 against the interfering mycotoxins (Ochratoxin and Fumonisin B1) was observed, and the obtained aptasensor has been successfully applied to analyze AFB_1 in the spiked wine samples to demonstrate its practicability. Voltammetric lipopolysaccharide (LPS) aptasensor on GCE has been fabricated by taking advantage of rGO/MoS_2 composite, which was functionalized with polyethyleneimine (PEI).[88] The resulting PEI/rGO/MoS_2 as a nanocarrier of electroactive toluidine blue (TB) was further decorated with AuNPs to immobilize thiolated LPS aptamer for amplifying the electrochemical signal of TB. Finally, the authors used bovine serum albumin (BSA) to block excess binding sites of the modified electrode. The process of the aptasensor preparation is displayed in **Figure 12**. The TB reduction signal (–0.35 V vs SCE) was inversely proportional to the concentrations of LPS in a linear range between 5.0×10^{-5} and 2.0×10^{2} ng mL^{-1} with the LOD of 3.01×10^{-5} ng mL^{-1}. The excellent performance was achieved by a large specific surface area, thermal stability, and electrical conductivity of GO/MoS_2, and the good biocompatibility of AuNPs. In addition, good selectivity for LPS was observed against the serum interferents BSA, dopamine (DA), ascorbic acid (AA), or glucose. Chekin et al. reported human papillomavirus (HPV) aptasensor based on modified porous rGO/MoS_2 for detecting HPV-16 via its L1 capsid protein.[155] They drop-casted porous rGO and MoS_2 sequentially on GCE, and then the modified electrode was functionalized using the mixture of poly(ethylene glycol) methyl ether thiol (HS-PEG) and 11-mercaptoundecanoic acid (MUA). MUA was used to link rGO/MoS_2 and L1 protein aptamer via carbodiimide chemistry (EDC/NHS). The ratio of MUA/HS-PEG was used to control the L1 aptamer density, and the best performance of the aptasensor was obtained at the ratio of 10/1. Then $[Fe(CN)_6]^{4-}$ as a redox /mediator was detected by DPV to quantify HPV-16 L1 protein. The corresponding current exhibited a linear decrease in the L1 protein concentration range of 0.2–2 ng mL^{-1} with LOD 0.1 ng mL^{-1}. The authors demonstrated that the good electronic properties and large surface area of graphene and MoS_2 improved electrochemical response.

An ultrasensitive electrochemical circulating tumor cells (CTCs) cytosensor benefited from the high surface area, fast electron transfer, and good biocompatibility of rGO/MoS_2 nanosheets was developed with Fe_3O_4 nanoparticles nanozyme

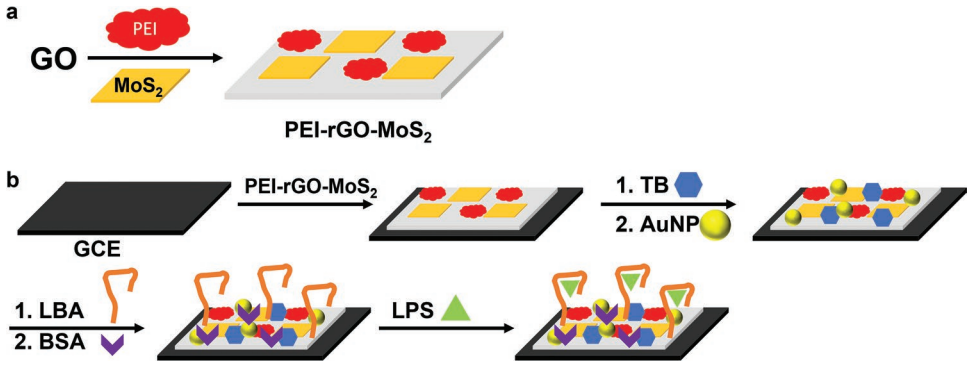

Figure 12. a) Illustration of the preparation of PEI–rGO–MoS_2. b) Schematic diagram of the modification process of the aptasensor.

to detect MCF-7.[156] The aptamer-modified superparamagnetic Fe_3O_4 NPs can be used to isolate and enrich CTCs. Moreover, Fe_3O_4 NPs as enzyme mimics and rGO/MoS_2 displayed the synergetic effect of reducing H_2O_2. Then the authors used 3,3′,5,5′-tetramethylbenzidine (TMB)–H_2O_2 system to detect cancer biomarkers at pH 5. Finally, the signal of TMB oxidation product (0.3 V vs SCE) was recorded using DPV measurements, and the as-prepared cytosensor displayed a linear range between 15 and 45 cells mL^{-1} with an LOD of 6 cells mL^{-1}. The schematic diagram of the enrichment of CTCs and cancer cell detection is displayed in **Figure 13**.

In addition, even without the help of biomolecules and metal nanoparticles, biosensors based on graphene and MoS_2, due to the large specific surface area and excellent electric conductivity, can also be employed to detect various biomolecules, such as AA, DA, uric acid (UA), and folic acid (FA). In 2015, Xing and Ma reported a MoS_2/rGO modified GCE to detect AA, DA, and UA, which displayed only a broad, overlapped, and very small anodic peak at bare GCE.[157] In this work, MoS_2/rGO was synthesized by a one-pot hydrothermal process. Three separated oxidation peaks at –64, 168, and 320 mV (vs Ag/AgCl) in DPV measurements correspond to the species mentioned above, respectively, attributed to improved conductivity and catalytic activity of MoS_2/rGO. Meanwhile, they obtained calibration curves with a linear range of 12–5402, 5–545, and 25–2745 μM and LOD of 0.72, 0.05, and 0.46 μM (S/N = 3) for AA, DA, and UA, respectively. The recoveries ranging from 98.9% to 104.1% (for n = 3) were observed for detecting these three

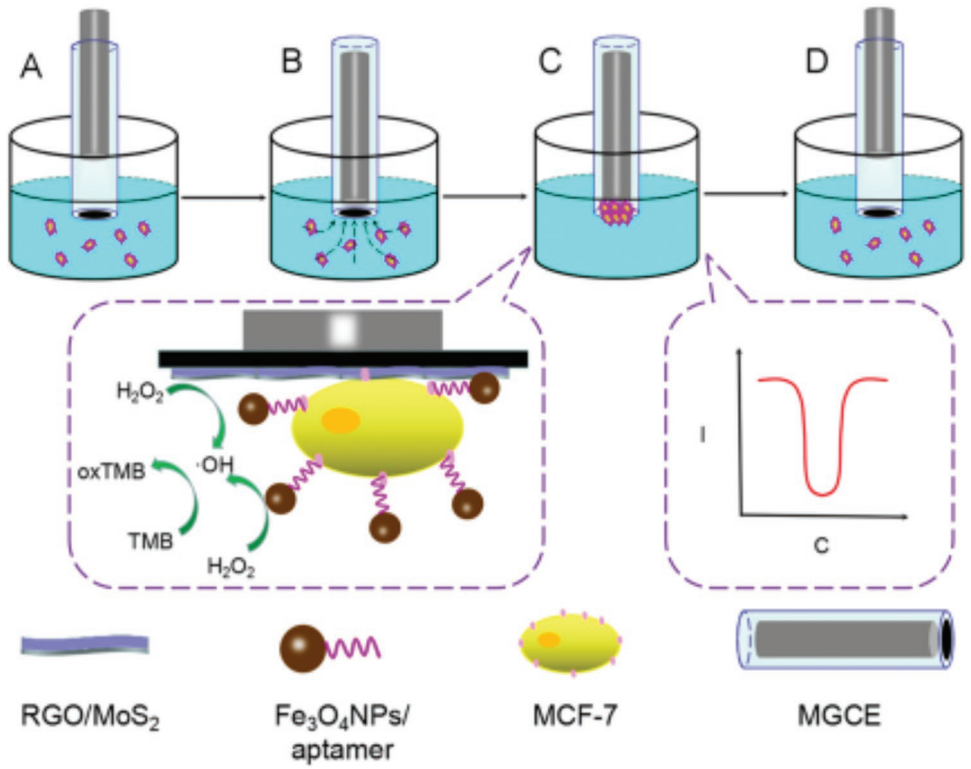

Figure 13. The schematic diagram of the cytosensor preparation and cancer cell detection. Reproduced with permission.[156] Copyright 2018, Elsevier B.V.

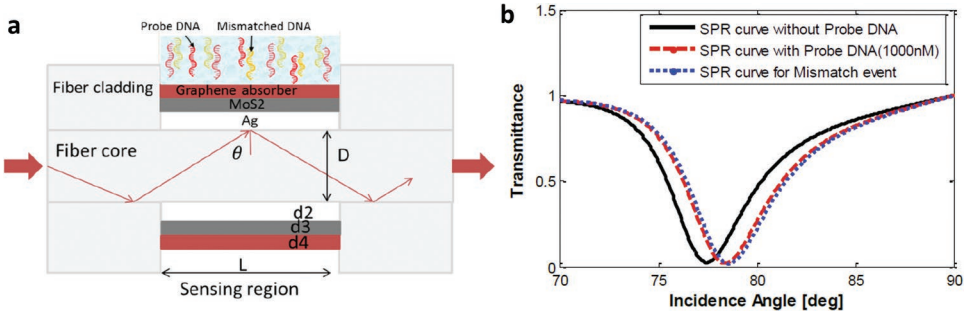

Figure 14. Sensing probe DNA and mismatched DNA hybridization by the proposed fiber–Ag–MoS_2–graphene SPR biosensor: a) schematic of the 5-layer model and b) comparison of SPR curves with and without DNA molecules (SPR angle is 77.45° for bare sensor, black line, 78.40° after adding only probe DNA, dashed red line, and 78.50° after immersing mismatched DNA, dotted blue line). Reproduced with permission.[166] Copyright 2017, Elsevier GmbH.

species in spiked human serum samples. More recently, VDWs stacks of MoS_2/graphene heterostructure with graphene on top were developed via a layer-by-layer transfer method.[158] The as-prepared sensor showed a linear range from 2.5 to 600 µmol L^{-1} for DA. Kıranşan and Topçu prepared a flexible and free-standing MoS_2/rGO composite paper as the biosensor to determine FA.[159] Cyclic voltammetry and amperometry were used to evaluate its electrocatalytic activity toward the FA. The oxidation current density linearly increased with the FA concentration in the range of 1.03×10^{-7}–1.24×10^{-3} M with an LOD of 3.68×10^{-8} M. Meanwhile, they obtained the recoveries of FA in serum samples in the range from 100.4% to 108% with small RSD from 0.7% to 4.3%, demonstrating the amperometric FA sensor is suitable for FA detection in real serum samples.

In Table 3 we summarized all electrochemical sensors discussed in this section of the review, with indicated the synthetic methods utilized as well as the principal figures of merit of each sensor (sensing platform, synthesis method, sensitivity, selectivity, response times, LOD).

5. SPR Biosensors

Over the last decades, SPR biosensors have attracted increasing attention for biosensing, such as DNA hybridization, owing to their fast response and high sensitivity.[160] SPR, known as the oscillating quantum of charge density at the metal–dielectric interface excited by TM-polarized electromagnetic waves, is very sensitive to changes in the surrounding RI.[161] Generally, the sensing medium and the dielectric are isolated by a thin metallic film (gold or silver) coated on the prism or fiber base in SPR sensors. Strong coupling at the metallic/graphene interface caused by the effective charge transfer leads to an enhanced electric field, which is also sensitive to the RI change of its surrounding media.[162,163] In addition, high carrier mobility, large surface area, and good absorption efficiency of graphene and MoS_2 endow them as idea substrates in SPR-based biosensors.[164,165] For the graphene/MoS_2-based SPR biosensors, the MoS_2/graphene layer is used as a biomolecular recognition element and is inserted between the metal layer and sensing medium to improve the sensitivity. Graphene is usually placed on top of MoS_2 and acts as a protection layer to prevent the reaction of MoS_2 with O_2 and water in the ambient environment or detecting solution. Hitherto, some groups have examined SPR-based biosensors with graphene/MoS_2 by theoretical and experimental investigations. In 2017, Rahman et al. proposed an optical fiber-based Ag/MoS_2/graphene hybrid SPR biosensor to detect DNA hybridization.[166] In this theoretical work, the authors deeply studied the sensitivity, detection accuracy, and quality factor. The inserted single MoS_2 layer displayed reasonable detection accuracy (1.626 RIU^{-1}) and quality factor (23.23 RIU^{-1}) for the sensitivity of 105.71° RIU^{-1}, which is 28.69% higher than that of conventional graphene-on-Ag SPR biosensors (86.43° RIU^{-1}). The improved sensitivity is ascribed to graphene's high absorption ability and optical characteristics and the high fluorescence quenching that originated from MoS_2. Meanwhile, the absence of hydrogen bonds caused by the mismatched pair between the probe and target DNA strands leads to negligible variations of resonance angle and spectrum of transmitted power, resulting in high selectivity. The selectivity of the proposed fiber/Ag/MoS_2/graphene SPR biosensor is shown in **Figure 14**. The same group also developed an SPR biosensor based on Au/MoS_2/graphene with a similar enhanced sensitivity and selectivity mechanism.[167] The sensitivity of the proposed SPR biosensor with 50 nm Au layer is 87.8° RIU^{-1} with detection accuracy and quality factor of 1.28 and 17.56 RIU^{-1}, respectively. Aksimsek et al. confirmed the conclusion of enhanced sensitivity led by the introduced graphene/MoS_2 heterostructures.[168] They theoretically demonstrated graphene/MoS_2/Ag angular SPR sensors with higher sensitivity by incorporating MoS_2 layers.

Apart from graphene and MoS_2, other 2D materials, such as BP, $MoSe_2$, WS_2, and WSe_2, have also demonstrated the capacity of improvement for SPR sensitivity owing to their unique electrical and optical properties. Few-layer BP with high carrier mobility, outstanding electrical, optical, and phonon properties have been integrated into the SPR biosensors with different 2D materials to enhance the sensitivity.[169] Since BP easily gets oxidized, five layers of graphene, monolayer MoS_2, monolayer WS_2, bilayer $MoSe_2$, or bilayer WSe_2 as the protective layer were coated on the surface of 5 nm thick BP, and the resulting SPR biosensors displayed the sensitivity of 217, 218, 237, 229, and 279° RIU^{-1}, respectively. This high sensitivity was achieved because the few-layer BP enhanced the electric field at the interface of the sensor/sensing medium and the light absorption of graphene. SPR-based fiber optic biosensors

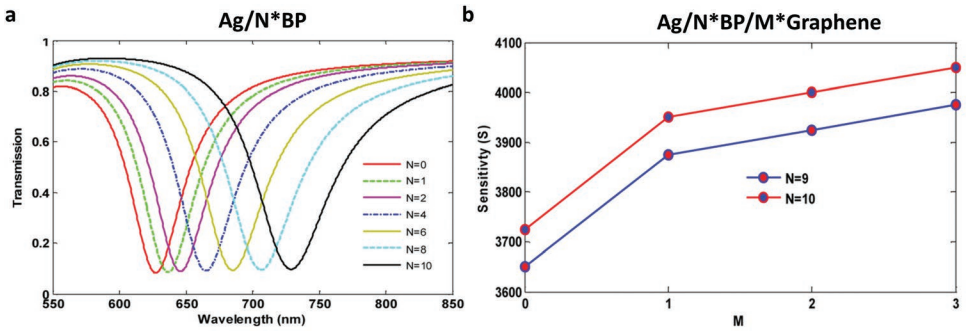

Figure 15. a) Variation in the transmittance as the function of the wavelength for different numbers of black phosphorene (BP) layers over the Ag film. b) Variation in the sensitivity with the number of graphene layers (M). Reproduced with permission.[170] Copyright 2019, Elsevier B.V.

with phosphorene and other 2D materials (graphene, MoS_2, WS_2, $MoSe_2$, and WSe_2) were theoretically designed to detect DNA hybridization.[170] The authors investigated the effect of phosphorene layers on performance parameters and achieved the highest sensitivity of 4050 nm RIU^{-1} for a heterostructure with ten-layer phosphorene and three-layer graphene (**Figure 15**), which is higher than that without graphene integration (3725 nm RIU^{-1}). The sensitivity was improved by the additional relatively high refractive index layer in the SPR biosensor and protective layers for preventing BP surface from oxidation.

Although Ag-coated SPR sensor generally shows higher sensitivity, Ag is not stable and easily undergoes oxidization and corrosion in distinct circumstances.[171] Therefore, other metal-based SPR sensors have also been proposed. Zeng et al. created an SPR biosensor based on Au and graphene–MoS_2 heterostructures.[165] In this theoretical study, the 45 nm Au thin film coated by three-layer MoS_2, and monolayer graphene structure are the optimal parameters to show the highest detection sensitivity range, since the Au/MoS_2 structure can improve the light absorption and SPR excitation. Meanwhile, monolayer graphene is a biorecognition component for targeting biomolecules detection via π-stacking interaction. A localized surface plasmon resonance biosensor based on MoS_2–graphene was proposed to detect DNA.[172] The schematic representation of the AuNPs/MoS_2/graphene sensor is shown in **Figure 16**, and the resulting sensor displayed a significantly improved sensitivity compared to that without MoS_2 and graphene. In the optimized structure of eight-layer MoS_2 and ten-layer graphene, the highest sensitivity of 360 nm RIU^{-1} was achieved due to their large surface-to-volume ratio, and their strong conductivity. Furthermore, the sensitivity is tuneable by the number of MoS_2 and graphene layers in SPR sensors. Mishra et al. performed a comparative theoretical study of SPR sensors of Au/graphene/MoS_2, Cu/graphene/MoS_2, and Al/graphene/MoS_2 configurations.[161] They demonstrated that Cu/graphene/MoS_2 and Al/graphene/MoS_2 possessed a higher sensitivity of 6.2 µm RIU^{-1} than Au/graphene/MoS_2 with 5.0 µm RIU^{-1}. TiO_2–SiO_2 composite layer between the prism base and the metal layer was used to enhance the sensitivity of the graphene/MoS_2-based SPR sensor due to the plasmonic effect near TiO_2–SiO_2 interface.[173] The proposed TiO_2–SiO_2–Au–graphene/MoS_2 sensor showed 3.28% higher sensitivity respected to the graphene–MoS_2-based SPR sensor. The same strategy was applied to simulate the detection of formaldehyde.[174] The authors obtained graphene/MoS_2/TiO_2–SiO_2 with higher sensitivity of 82.5% compared to 80.5% of only graphene/MoS_2 due to the rich plasmon at the TiO_2–SiO_2 interface, which finally results in the enhanced sensitivity.

All the SPR biosensors discussed in this section of the review were summarized in Table 4, with indicated the synthetic methods utilized as well as the principal figures of merit of each sensor (sensing platform, type of work, sensitivity, analyte, detection accuracy, quality factor)

5.1. Other Biosensors

Besides electrochemistry, during the last few years, biosensors based on other technologies, such as FET and photoluminescence, have been developed. Chen et al. proposed FET biosensors based on MoS_2/graphene hybrid nanostructure for detecting DNA hybridization.[176] The 1-pyrenebutanoic acid succinimidyl ester was used as the linker between the 5′-amine-modified Probe DNA and the MoS_2/graphene via a conjugated reaction to immobilize the Probe DNA (**Figure 17**a). The authors utilized the voltage shift of the charge-neutral point (ΔV_{CNP}) and the change of drain current (ΔI_{ds}) of the MoS_2/graphene FET sensor to detect DNA hybridization and obtain a broad response range between 10 aM and 100 pM with a low LOD of 10 aM. The LOD was one or more orders of magnitude lower than the previously reported result. MoS_2 layers in the hybrid resulted in a stronger donor effect and a weaker gating effect, leading to a larger ΔV_{CNP}. Moreover, the high specificity for different complementary DNA indicates that the FET sensor might be used in disease diagnosis. On the basis of PL measurement with a confocal system, graphene/CVD MoS_2 hybrid stacking film was used as the substrate or label-free and selective detection of DNA hybridization.[177] The graphene layer on the top of MoS_2 acted as a protection layer for unstable ambient MoS_2 and a biocompatible interface layer for DNA hosting. The schematic illustration of the graphene/MoS_2 biosensor is shown in Figure 17b. The PL intensity of the MoS_2 layer in the hybrid increases with the concentration of the added target DNA while not with the mismatched DNA. They obtained the linear range from 1 aM to 1 fM with LOD at aM level.

In addition to graphene/MoS_2 heterostructures, a novel photoelectrochemical (PEC) biosensor based on MoS_2/WS_2 heterojunction nanocomposite was reported by Li et al. for

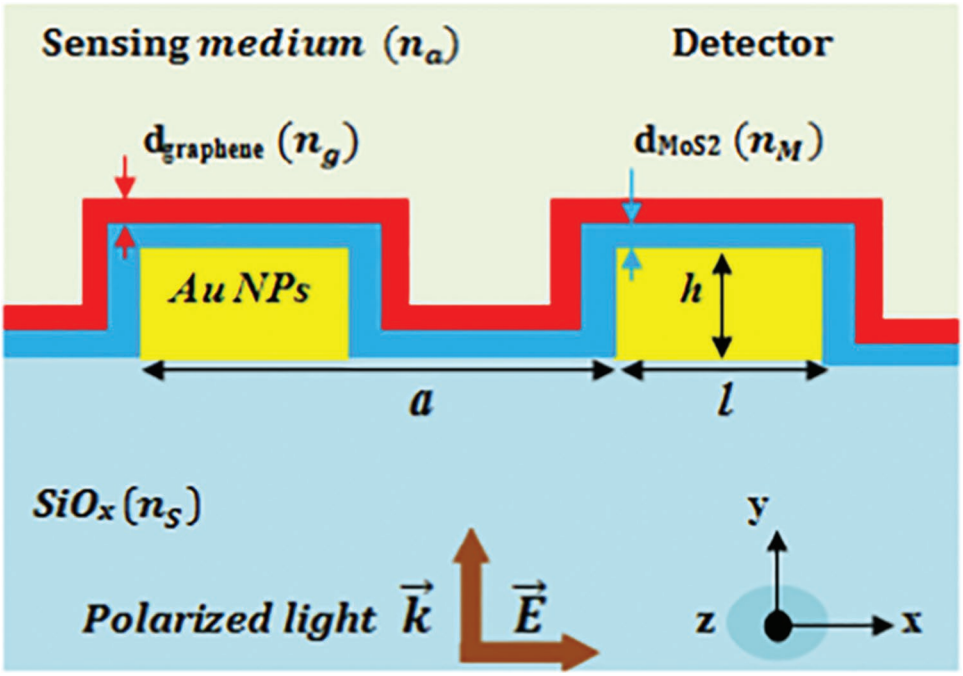

Figure 16. Schematic representation of AuNPs when covered with few layers of MoS_2/graphene and another dielectric lying on top (detection medium of refraction index n_a) and deposited on a SiO_x substrate (SiO_x/AuNPs/MoS_2/graphene/dielectric). The particles form a 1D grating along *x*-axis. The AuNPs grating is characterized by parameter *h* referring to the particle's height, *l* is their length, and *a* is the lattice parameter. The input wave source (monochromatic plane wave) is also shown. Reproduced with permission.[172] Copyright 2020, Elsevier Ltd. Besides the theoretical study of sensing DNA hybridization, an experimental work on a D-shaped fiber SPR sensor based on a CVD MoS_2/CVD graphene was developed for the detection of glucose. Reproduced with permission.[175] Copyrights 2020, Elsevier B. V. They functionalized graphene with pyrene-1-boronic acid (PBA) via π–π stacking interactions to realize the selectivity and utilized gold film to excite the SPR effect. In addition, the sensitivity of the sensors is dependent on the number of MoS_2 layers. In this work, the as-obtained biosensor with three-layer MoS_2 and monolayer graphene demonstrated the highest sensitivity of 6708.87 nm RIU^{-1}, as well as good selectivity of glucose against UA, AA, and DA with a concentration of 0.1 mM.

determining 5-formylcytosine (5fC) in mammalian DNA.[178] The final biosensor incorporated MoS_2/WS_2 as a photoactive material, 4-Amino-3-hydrazino-5-mercapto-1,2,4-triazole as a linker, and black TiO_2 (B-TiO_2) was used as a signal amplification unit. They used WS_2 to improve the photoactivity of MoS_2 due to the matched energy band. Figure 17c shows the schematic illustration of the preparation process of the PEC biosensor. The acceptable stability of the PEC biosensor was proved by monitoring the photocurrent, with the RSD only 1.48% during 10 cycles. The as-prepared PEC biosensor demonstrated a linear range of 0.01 to 200 nM and an LOD of 2.7 pM (S/N = 3). Moreover, the proposed biosensor is highly sensitive and allows the quantitative study of 5fC content in roots, stems, and leaves of maize seedlings affected by Cr^{2+}.

In **Table 5** we summarized all the sensors discussed in this section of the review, with indicated the synthetic methods utilized as well as the principal figures of merit of each sensor (sensing platform, synthesis method, testing method, analyte, LOD).

6. Conclusion and Perspective

In this review article, we provided an insight into the promising application of hybrids of two or more 2D materials, better known as VDWHs, in the sensing of different chemicals, including DNA, AA, and DA. Indeed, sensors have paramount importance in the era of the internet of things and have a

Table 5. Summary of the VDWHs for biosensors in this section.

Other sensors					
Sensing platform	Preparation	Testing method	Target	LOD	Refs.
MoS_2/graphene	Mechanical transfer	FET sensor	DNA	10 aM	[176]
Graphene/CVDMoS_2	Mechanical transfer	Photoluminescence sensor	DNA	1 aM	[177]
ITO/$MoS_2/WS_2/Fe_3O_4$	Drop-casting	Photoelectrochemical (PEC) biosensor	DNA	2.7 pM	[178]

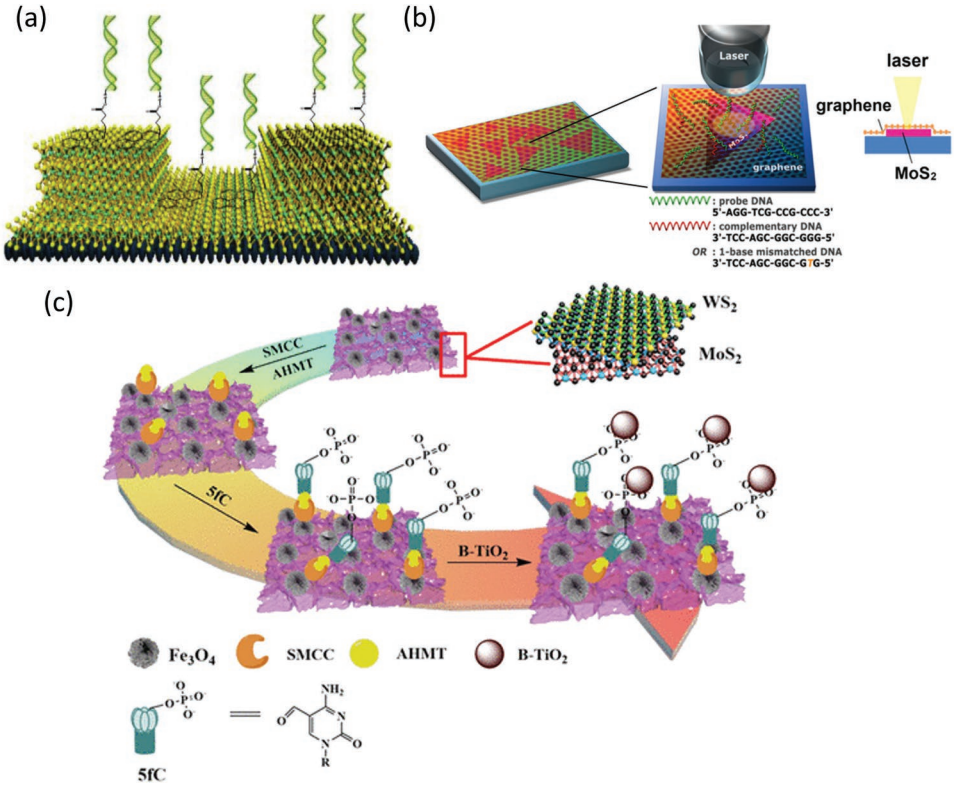

Figure 17. a) Schematic of the MoS_2/graphene nanostructure. Reproduced with permission.[176] Copyright 2020, Elsevier B.V. b) Schematic illustration of the DNA detection method using a microscope and the graphene/MoS_2 heterostructure sensor. c) Schematic illustration of the construction process of the proposed PEC biosensor. Reproduced with permission.[178] Copyright 2020, American Chemical Society.

fundamental role in improving our quality of life. Gas chemical sensors and biosensors allow monitoring of our health, the quality of the air we breathe, the water we drink, or the food we eat and also are important tools for medical diagnosis, such as target DNA detection.

2D materials are appealing candidates for sensing by virtue of their large surface-to-area ratios in the first instance, which assure plenty of room for the analytes to interact with the 2D material and thus be sensed. Second, the electrical conductivity of graphene and TMDs enables the interaction of the 2D material with the analyte to be easily measured as changes in the electrical properties. Nevertheless, the lack of a tuneable bandgap and the inertness of pristine graphene are the reasons for its low and poorly selective sensitivity. On the other hand, TMDs and phosphorene have tuneable bandgaps and more reactive surfaces, which make these materials' theoretical sensitivity higher than graphene. Yet, the same reactivity is the reason for the low environmental and long-term stability of these 2D materials. Graphene can be combined with other 2D materials, increasing stability, and improving electrical conductivity. Furthermore, the sensing performances can be greatly enhanced by a synergistic effect when two (or more) 2D materials are combined to form VDWHs. For instance, combining semiconductive 2D materials with different work functions leads to p–n junctions forming, which produces a huge increase in sensitivity. Similarly, Schottky junctions formed by combining graphene with semiconducting 2D materials also have a positive impact on the sensitivity. For biosensors, graphene can play as a protection layer for air-sensitive MoS_2, improving the stability of the resulting devices. Another potential advantage of VDWH is that the number of them that could be formed is enormous if we consider all the 2D materials already available and all the possible combinations between them. Each of these different VDWHs could target the analyte of interest specifically and selectively. Moreover, the selectivity and sensitivity toward the target analyte can be further increased by more than two different 2D materials with/without functional nanoparticles and specific binding molecules such as antibodies, enzymes, and aptamers. Considering that more than 1000 different layered VDW materials, which can be exfoliated have been predicted, with diverse physical and chemical properties, we believe that machine learning would be a helpful strategy for rational design and high throughput screening of 2D VDW heterostructures. Systemic and comparative studies with different 2D VDWHs for the same target analyte would help one better understand the potential and limits of heterostructures and facilitate optimizing the final sensors. Nonetheless, despite the promising properties, some significant challenges still need to be tackled to make VDWHs competitive in the industrial market. The major drawback is the method used to form many of the VDW, which consists of time-consuming and non-scalable steps. Indeed, up to now, many VDWs are based on mechanically exfoliated monolayer (or few-layer) flakes which are stacked together through complicated transfer processes. CVD processes are slightly more scalable yet are very expensive. On the contrary, heterostructures produced by cheaper, easier, and higher throughput processes, such as mixing of liquid-phase exfoliated material, sol–gel processing, and liquid-phase

functionalization, may have an important advantage toward industrialization. In addition, the mechanism of VDWHs for biosensing is still not very clear; most of the literature stated that the better performance of VDWHs is due to their synergistic effects. However, only a few of them provided convincing proof. Therefore, more detailed and systematic mechanistic studies are still required in order to provide a theoretical basis for involving new sensors. To exploit 2D VDWHs in everyday applications, the researchers need to develop industrial-scalable and affordable manufacturing approaches, maintaining the high KPIs of sensors. New computational works, supported by experimental evidence, which cast light onto a deeper understanding of the relationship between sensor performances and material parameters (e.g., number of layers, crystallinity, porosity) are desirable. The recently reported strategies of exfoliated 2D materials, e.g., intercalation graphite compounds, may be an efficient method to fabricate VDWHs, which is not only suitable for chemical sensing but also in other applications, such as more broadly optoelectronics (e.g., FETs) and energy storage (viz., batteries). Meanwhile, the use of liquid-phase methods of ease scalability and low cost to produce specific ordered 2D heterostructures still represents a major challenge that requires more in-depth studies. Further challenges associated with upgrading 2D VDWHs from the prototype (laboratory) to commercial sensing technologies involve the affordable price of the final product, user-friendly (no need for complex training), low power consumption, and long-term sensor reliability in daily operation.

The layer numbers of 2D materials are another critical parameter for the sensitivity of 2D VDWHs sensors. Fewer layer thickness can increase the specific surface area but also reduce light absorption and reflection, which is considered, in particular, in SPR biosensors. Meanwhile, different 2D materials vertical stack can lead to structural deformities, which affect their electronic properties and may have positive or negative responses of sensors depending on the specific applications. Therefore, theoretical calculations in situ and/or high-resolution transmission electron microscopy, and other spectroscopic methods (such as Raman and X-ray photoelectron spectroscopy) would be needed in the synthesis of 2D VDWHs to elucidate these changes in properties caused by stacking.

On the other hand, in view of the key role of functionalization of the 2D materials and the VDWHs thereof with the receptor of the analyte of choice, advances in the controlled chemical functionalization of 2D materials will be extremely beneficial for sensing applications. The rich chemistry of 2D materials surface endows multifunctional group/receptor, which can be used to detect different targets simultaneously. Moreover, synchronization of detection and treatment is possible with drug loading/delivery on the sensor. Finally, efforts on the integration of the developed sensors in flexible and portable technologies, powered with low voltages, or self-powered will be key to developing point-of-care devices for medical diagnosis and well-being.

Acknowledgements

The authors gratefully acknowledge the financial support from the University of Trieste, INSTM, the Italian Ministry of Education MIUR (Cofin Prot. 2017PBXPN4) and the Maria de Maeztu Units of Excellence Program from the Spanish State Research Agency (Grant No. MDM-2017-0720). The authors acknowledge financial support from the EC through the Graphene Flagship Core 3 project (GA-881603) and the ERC project SUPRA2DMAT (GA-833707), the Interdisciplinary Thematic Institute SysChem via the IdEx Unistra (ANR-10-IDEX-0002) within the program Investissement d'Avenir program, the International Center for Frontier Research in Chemistry and the Institut Universitaire de France (IUF). M.P. is AXA Chair of Bionanotechnology. A.C. thanks MINECO and Xunta de Galicia for his research grants (Ramon y Cajal No. RYC2020-030183-I, and Atracción de Talento No. ED431H 2020/17, respectively). H.-L.H. thanks MINECO for his research grant (Juan de la Cierva Incorporacion/No. IJC-2018-037396-I).

Open access funding provided by Universita degli Studi di Trieste within the CRUI-CARE Agreement.

Conflict of Interest

The authors declare no conflict of interest.

Keywords

2D materials, sensors, van der Waals heterostructures

Received: June 21, 2022
Revised: August 21, 2022
Published online: October 10, 2022

[1] S. Yao, P. Ren, R. Song, Y. Liu, Q. Huang, J. Dong, B. T. O'Connor, Y. Zhu, *Adv. Mater.* **2020**, *32*, 1902343.
[2] J.-H. Hsiao, Y.-T. Tsao, C.-Y. Yang, C.-M. Cheng, in *Chemical, Gas, and Biosensors for Internet of Things and Related Applications* (Eds.: K. Mitsubayashi, O. Niwa, Y. Ueno), Elsevier, New York **2019**, pp. 13–26.
[3] T. M. Swager, K. A. Mirica, *Chem. Rev.* **2019**, *119*, 1.
[4] M. V. Nikolic, V. Milovanovic, Z. Z. Vasiljevic, Z. Stamenkovic, *Sensors* **2020**, *20*, 6694.
[5] M. Holzinger, A. L. Goff, S. Cosnier, *Front. Chem.* **2014**, *2*, 1.
[6] A. Bolotsky, D. Butler, C. Dong, K. Gerace, N. R. Glavin, C. Muratore, J. A. Robinson, A. Ebrahimi, *ACS Nano* **2019**, *13*, 9781.
[7] M. Mathew, P. V. Shinde, R. Samal, C. S. Rout, *J. Mater. Sci.* **2021**, *56*, 9575.
[8] C. Cheng, S. Li, A. Thomas, N. A. Kotov, R. Haag, *Chem. Rev.* **2017**, *117*, 1826.
[9] Z. Meng, R. M. Stolz, L. Mendecki, K. A. Mirica, *Chem. Rev.* **2019**, *119*, 478.
[10] X. Wang, Y. Zhang, J. Wu, Z. Zhang, Q. Liao, Z. Kang, Y. Zhang, *Chem. Rev.* **2022**, *122*, 1273.
[11] L. Li, W. Han, L. Pi, P. Niu, J. Han, C. Wang, B. Su, H. Li, J. Xiong, Y. Bando, T. Zhai, *InfoMat* **2019**, *1*, 54.
[12] J. Azadmanjiri, V. K. Srivastava, P. Kumar, Z. Sofer, J. Min, J. Gong, *Appl. Mater. Today* **2020**, *19*, 100600.
[13] F. Xia, H. Wang, D. Xiao, M. Dubey, A. Ramasubramaniam, *Nat. Photonics* **2014**, *8*, 899.
[14] C. Lee, X. Wei, J. W. Kysar, J. Hone, *Science* **2008**, *321*, 385.
[15] Y. Zhang, Y. W. Tan, H. L. Stormer, P. Kim, *Nature* **2005**, *438*, 201.
[16] J. H. Gosling, O. Makarovsky, F. Wang, N. D. Cottam, M. T. Greenaway, A. Patanè, R. D. Wildman, C. J. Tuck, L. Turyanska, T. M. Fromhold, *Commun. Phys.* **2021**, *4*, 30.
[17] A. Chaves, J. G. Azadani, H. Alsalman, D. R. da Costa, R. Frisenda, A. J. Chaves, S. H. Song, Y. D. Kim, D. He, J. Zhou, A. Castellanos-Gomez, F. M. Peeters, Z. Liu, C. L. Hinkle, S.-H. Oh,

P. D. Ye, S. J. Koester, Y. H. Lee, P. Avouris, X. Wang, T. Low, *npj 2D Mater. Appl.* **2020**, *4*, 29.
[18] H. Qiao, H. Liu, Z. Huang, R. Hu, Q. Ma, J. Zhong, X. Qi, *Energy Environ. Mater.* **2021**, *4*, 522.
[19] S. Manzeli, D. Ovchinnikov, D. Pasquier, O. V. Yazyev, A. Kis, *Nat. Rev. Mater.* **2017**, *2*, 17033.
[20] K. F. Mak, C. Lee, J. Hone, J. Shan, T. F. Heinz, *Phys. Rev. Lett.* **2010**, *105*, 2.
[21] Y. Wang, Y. Shao, D. W. Matson, J. Li, Y. Lin, *ACS Nano* **2010**, *4*, 1790.
[22] K. Kalantar-zadeh, J. Z. Ou, *ACS Sens.* **2016**, *1*, 5.
[23] V. Georgakilas, J. N. Tiwari, K. C. Kemp, J. A. Perman, A. B. Bourlinos, K. S. Kim, R. Zboril, *Chem. Rev.* **2016**, *116*, 5464.
[24] G. Reina, J. M. González-Domínguez, A. Criado, E. Vázquez, A. Bianco, M. Prato, *Chem. Soc. Rev.* **2017**, *46*, 4400.
[25] N. Alzate-Carvajal, A. Luican-Mayer, *ACS Omega* **2020**, *5*, 21320.
[26] D. Tyagi, H. Wang, W. Huang, L. Hu, Y. Tang, Z. Guo, Z. Ouyang, H. Zhang, *Nanoscale* **2020**, *12*, 3535.
[27] A. A. Avetisyan, B. Partoens, F. M. Peeters, *Phys. Rev. B* **2009**, *79*, 35421.
[28] M. Zeng, Y. Xiao, J. Liu, K. Yang, L. Fu, *Chem. Rev.* **2018**, *118*, 6236.
[29] S. Z. Butler, S. M. Hollen, L. Cao, Y. Cui, J. A. Gupta, H. R. Gutiérrez, T. F. Heinz, S. S. Hong, J. Huang, A. F. Ismach, E. Johnston-Halperin, M. Kuno, V. V Plashnitsa, R. D. Robinson, R. S. Ruoff, S. Salahuddin, J. Shan, L. Shi, M. G. Spencer, M. Terrones, W. Windl, J. E. Goldberger, *ACS Nano* **2013**, *7*, 2898.
[30] C. W. Lee, J. M. Suh, H. W. Jang, *Front Chem* **2019**, *7*, 1.
[31] S. Barua, H. S. Dutta, S. Gogoi, R. Devi, R. Khan, *ACS Appl. Nano Mater.* **2018**, *1*, 2.
[32] A. Nag, A. Mitra, S. C. Mukhopadhyay, *Sens. Actuators, A* **2018**, *270*, 177.
[33] W. J. Peveler, M. Yazdani, V. M. Rotello, *ACS Sens.* **2016**, *1*, 1282.
[34] R. Furlan de Oliveira, V. Montes-García, A. Ciesielski, P. Samorì, *Mater. Horiz.* **2021**, *8*, 2685.
[35] C. Anichini, W. Czepa, D. Pakulski, A. Aliprandi, A. Ciesielski, P. Samorì, *Chem. Soc. Rev.* **2018**, *47*, 4860.
[36] K. Khan, A. K. Tareen, M. Aslam, R. Wang, Y. Zhang, A. Mahmood, Z. Ouyang, H. Zhang, Z. Guo, *J. Mater. Chem. C* **2020**, *8*, 387.
[37] F. Bonaccorso, L. Colombo, G. Yu, M. Stoller, V. Tozzini, A. C. Ferrari, R. S. Ruoff, V. Pellegrini, *Science* **2015**, *347*, 1246501.
[38] F. Schedin, A. K. Geim, S. V. Morozov, E. W. Hill, P. Blake, M. I. Katsnelson, K. S. Novoselov, *Nat. Mater.* **2007**, *6*, 652.
[39] R. Bogue, *Sens. Rev.* **2014**, *34*, 233.
[40] A. Ghosh, A. I. Chizhik, N. Karedla, J. Enderlein, *Nat. Protoc.* **2021**, *16*, 3695.
[41] F. Wang, Y. Zhang, C. Tian, C. Girit, A. Zettl, M. Crommie, Y. R. Shen, *Science* **2008**, *320*, 206.
[42] Q. Ye, J. Wang, Z. Liu, Z. C. Deng, X. T. Kong, F. Xing, X. D. Chen, W. Y. Zhou, C. P. Zhang, J. G. Tian, *Appl. Phys. Lett.* **2013**, *102*, 021912.
[43] F. Xing, G.-X. Meng, Q. Zhang, L.-T. Pan, P. Wang, Z.-B. Liu, W.-S. Jiang, Y. Chen, J.-G. Tian, *Nano Lett.* **2014**, *14*, 3563.
[44] F. Xing, Z.-B. Liu, Z.-C. Deng, X.-T. Kong, X.-Q. Yan, X.-D. Chen, Q. Ye, C.-P. Zhang, Y.-S. Chen, J.-G. Tian, *Sci. Rep.* **2012**, *2*, 908.
[45] S. S. Kwon, J. Yi, W. W. Lee, J. H. Shin, S. H. Kim, S. H. Cho, S. Nam, W. Il Park, *ACS Appl. Mater. Interfaces* **2016**, *8*, 834.
[46] A. Béraud, M. Sauvage, C. M. Bazán, M. Tie, A. Bencherif, D. Bouilly, *Analyst* **2021**, *146*, 403.
[47] M. Zhou, Y. Zhai, S. Dong, *Anal. Chem.* **2009**, *81*, 5603.
[48] M. J. Allen, V. C. Tung, R. B. Kaner, *Chem. Rev.* **2010**, *110*, 132.
[49] N. Mounet, M. Gibertini, P. Schwaller, D. Campi, A. Merkys, A. Marrazzo, T. Sohier, I. E. Castelli, A. Cepellotti, G. Pizzi, N. Marzari, *Nat. Nanotechnol.* **2018**, *13*, 246.
[50] D. Le, T. B. Rawal, T. S. Rahman, *J. Phys. Chem. C* **2014**, *118*, 5346.
[51] D. Lembke, S. Bertolazzi, A. Kis, *Acc Chem Res* **2015**, *48*, 100.
[52] N. Yu, L. Wang, M. Li, X. Sun, T. Hou, Y. Li, *Phys. Chem. Chem. Phys.* **2015**, *17*, 11700.
[53] Y. Zhang, D. Feng, Y. Xu, Z. Yin, W. Dou, U. E. Habiba, C. Pan, Z. Zhang, H. Mou, H. Deng, X. Mi, N. Dai, *Appl. Surf. Sci.* **2021**, *548*, 149169.
[54] A. Splendiani, L. Sun, Y. Zhang, T. Li, J. Kim, C. Y. Chim, G. Galli, F. Wang, *Nano Lett.* **2010**, *10*, 1271.
[55] S. Catalán-Gómez, M. Briones, S. Cortijo-Campos, T. García-Mendiola, A. de Andrés, S. Garg, P. Kung, E. Lorenzo, J. L. Pau, A. Redondo-Cubero, *Sci. Rep.* **2020**, *10*, 16039.
[56] W. Zhang, P. Zhang, Z. Su, G. Wei, *Nanoscale* **2015**, *7*, 18364.
[57] X. Zhang, Z. Lai, C. Tan, H. Zhang, *Angew. Chem., Int. Ed.* **2016**, *55*, 8816.
[58] L. Yan, H. Shi, X. Sui, Z. Deng, L. Gao, *RSC Adv.* **2017**, *7*, 23573.
[59] J. Martincová, M. Otyepka, P. Lazar, *Chem. – Eur. J.* **2017**, *23*, 13233.
[60] J. Gao, B. Li, J. Tan, P. Chow, T. M. Lu, N. Koratkar, *ACS Nano* **2016**, *10*, 2628.
[61] J. W. Jiang, *Front. Phys.* **2015**, *10*, 287.
[62] J. W. Choi, J. Yoon, J. Lim, M. Shin, S. N. Lee, *Materials* **2021**, *14*, 518.
[63] E. Lee, Y. S. Yoon, D.-J. Kim, *ACS Sens.* **2018**, *3*, 2045.
[64] C. R. Dean, A. F. Young, I. Meric, C. Lee, L. Wang, S. Sorgenfrei, K. Watanabe, T. Taniguchi, P. Kim, K. L. Shepard, J. Hone, *Nat. Nanotechnol.* **2010**, *5*, 722.
[65] M. Yankowitz, J. Xue, D. Cormode, J. D. Sanchez-Yamagishi, K. Watanabe, T. Taniguchi, P. Jarillo-Herrero, P. Jacquod, B. J. Leroy, *Nat. Phys.* **2012**, *8*, 382.
[66] C. R. Dean, L. Wang, P. Maher, C. Forsythe, F. Ghahari, Y. Gao, J. Katoch, M. Ishigami, P. Moon, M. Koshino, T. Taniguchi, K. Watanabe, K. L. Shepard, J. Hone, P. Kim, *Nature* **2013**, *497*, 598.
[67] J. Jung, A. M. Dasilva, A. H. Macdonald, S. Adam, *Nat. Commun.* **2015**, *6*, 6308.
[68] A. K. Geim, I. V. Grigorieva, *Nature* **2013**, *499*, 419.
[69] H. Wang, F. Liu, W. Fu, Z. Fang, W. Zhou, Z. Liu, *Nanoscale* **2014**, *6*, 12250.
[70] P. Solís-Fernández, M. Bissett, H. Ago, *Chem. Soc. Rev.* **2017**, *46*, 4572.
[71] S. Bertolazzi, D. Krasnozhon, A. Kis, *ACS Nano* **2013**, *7*, 3246.
[72] K. Roy, M. Padmanabhan, S. Goswami, T. P. Sai, G. Ramalingam, S. Raghavan, A. Ghosh, *Nat. Nanotechnol.* **2013**, *8*, 826.
[73] F. Withers, O. Del Pozo-Zamudio, A. Mishchenko, A. P. Rooney, A. Gholinia, K. Watanabe, T. Taniguchi, S. J. Haigh, A. K. Geim, A. I. Tartakovskii, K. S. Novoselov, *Nat. Mater.* **2015**, *14*, 301.
[74] Y. Tsuboi, F. Wang, D. Kozawa, K. Funahashi, S. Mouri, Y. Miyauchi, T. Takenobu, K. Matsuda, *Nanoscale* **2015**, *7*, 14476.
[75] L. Peng, Y. Zhu, H. Li, G. Yu, *Small* **2016**, *12*, 6183.
[76] E. Pomerantseva, Y. Gogotsi, *Nat. Energy* **2017**, *2*, 17089.
[77] S. J. Haigh, A. Gholinia, R. Jalil, S. Romani, L. Britnell, D. C. Elias, K. S. Novoselov, L. A. Ponomarenko, A. K. Geim, R. Gorbachev, *Nat. Mater.* **2012**, *11*, 764.
[78] P. J. Zomer, S. P. Dash, N. Tombros, B. J. Van Wees, *Appl. Phys. Lett.* **2011**, *99*, 232104.
[79] L. Wang, I. Meric, P. Y. Huang, Q. Gao, Y. Gao, H. Tran, T. Taniguchi, K. Watanabe, L. M. Campos, D. A. Muller, J. Guo, P. Kim, J. Hone, K. L. Shepard, C. R. Dean, *Science* **2013**, *342*, 614.
[80] G. Gao, W. Gao, E. Cannuccia, J. Taha-Tijerina, L. Balicas, A. Mathkar, T. N. Narayanan, Z. Liu, B. K. Gupta, J. Peng, Y. Yin, A. Rubio, P. M. Ajayan, *Nano Lett.* **2012**, *12*, 3518.
[81] J. Sun, H.-W. Lee, M. Pasta, H. Yuan, G. Zheng, Y. Sun, Y. Li, Y. Cui, *Nat. Nanotechnol.* **2015**, *10*, 980.
[82] X. Ling, Y.-H. Lee, Y. Lin, W. Fang, L. Yu, M. S. Dresselhaus, J. Kong, *Nano Lett.* **2014**, *14*, 464.
[83] Z. Liu, L. Song, S. Zhao, J. Huang, L. Ma, J. Zhang, J. Lou, P. M. Ajayan, *Nano Lett.* **2011**, *11*, 2032.

[84] X. Song, T. Gao, Y. Nie, J. Zhuang, J. Sun, D. Ma, J. Shi, Y. Lin, F. Ding, Y. Zhang, Z. Liu, *Nano Lett.* **2016**, *16*, 6109.
[85] M. Govindasamy, S. M. Chen, V. Mani, M. Akilarasan, S. Kogularasu, B. Subramani, *Microchim. Acta* **2017**, *184*, 725.
[86] Q. Feng, K. Duan, X. Ye, D. Lu, Y. Du, C. Wang, *Sens. Actuators, B* **2014**, *192*, 1.
[87] A. M. Villa-Manso, M. Revenga-Parra, M. Vera-Hidalgo, M. Vázquez Sulleiro, E. M. Pérez, E. Lorenzo, F. Pariente, *Sens. Actuators, B* **2021**, *345*, 130385.
[88] Y. Yuan, L. Li, M. Zhao, J. Zhou, Z. Chen, L. Bai, *Analyst* **2019**, *144*, 1253.
[89] G. F. Fine, L. M. Cavanagh, A. Afonja, R. Binions, *Sensors* **2010**, *10*, 5469.
[90] Y. Pak, S. M. Kim, H. Jeong, C. G. Kang, J. S. Park, H. Song, R. Lee, N. Myoung, B. H. Lee, S. Seo, J. T. Kim, G. Y. Jung, *ACS Appl. Mater. Interfaces* **2014**, *6*, 13293.
[91] S. J. Choi, B. H. Jang, S. J. Lee, B. K. Min, A. Rothschild, I. D. Kim, *ACS Appl. Mater. Interfaces* **2014**, *6*, 2588.
[92] J. Zhang, X. Liu, G. Neri, N. Pinna, *Adv. Mater.* **2016**, *28*, 795.
[93] C. Wang, L. Yin, L. Zhang, D. Xiang, R. Gao, *Sensors* **2010**, *10*, 2088.
[94] Y. L. Wang, X. C. Jiang, Y. N. Xia, *J. Am. Chem. Soc.* **2003**, *125*, 16176.
[95] S. A. Waghuley, S. M. Yenorkar, S. S. Yawale, S. P. Yawale, *Sens. Actuators, B* **2008**, *128*, 366.
[96] W. Yang, L. Gan, H. Li, T. Zhai, *Inorg. Chem. Front.* **2016**, *3*, 433.
[97] H. Hashtroudi, I. D. R. Mackinnon, M. Shafiei, *J. Mater. Chem. C* **2020**, *8*, 13108.
[98] B. Cho, A. R. Kim, D. J. Kim, H.-S Chung, S. Y. Choi, J.-D. Kwon, S. W. Park, Y. Kim, B. H. Lee, K. H. Lee, D.-H. Kim, J. Nam, M. G. Hahm, *ACS Appl. Mater. Interfaces* **2016**, *8*, 19635.
[99] B. Cho, J. Yoon, S. K. Lim, A. R. Kim, D. H. Kim, S. G. Park, J. D. Kwon, Y. J. Lee, K. H. Lee, B. H. Lee, H. C. Ko, M. G. Hahm, *ACS Appl. Mater. Interfaces* **2015**, *7*, 16775.
[100] B. Cho, M. G. Hahm, M. Choi, J. Yoon, A. R. Kim, Y. J. Lee, S. G. Park, J. D. Kwon, C. S. Kim, M. Song, Y. Jeong, K. S. Nam, S. Lee, T. J. Yoo, C. G. Kang, B. H. Lee, H. C. Ko, P. M. Ajayan, D. H. Kim, *Sci. Rep.* **2015**, *5*, 8052.
[101] Z. Li, Z. Yao, A. A. Haidry, Y. Luan, Y. Chen, B. Y. Zhang, K. Xu, R. Deng, N. Duc Hoa, J. Zhou, J. Z. Ou, *Nano Today* **2021**, *40*, 101287.
[102] A. Bag, N.-E. Lee, *J. Mater. Chem. C* **2019**, *7*, 13367.
[103] W. Zheng, X. Liu, J. Xie, G. Lu, J. Zhang, *Coord. Chem. Rev.* **2021**, *447*, 214151.
[104] L. H. Li, J. Cervenka, K. Watanabe, T. Taniguchi, Y. Chen, *ACS Nano* **2014**, *8*, 1457.
[105] Z. Liu, Y. Gong, W. Zhou, L. Ma, J. Yu, J. C. Idrobo, J. Jung, A. H. Macdonald, R. Vajtai, J. Lou, P. M. Ajayan, *Nat. Commun.* **2013**, *4*, 2541.
[106] R. A. Doganov, E. C. T. O'Farrell, S. P. Koenig, Y. Yeo, A. Ziletti, A. Carvalho, D. K. Campbell, D. F. Coker, K. Watanabe, T. Taniguchi, A. H. C. Neto, B. Özyilmaz, *Nat. Commun.* **2015**, *6*, 6647.
[107] G. Liu, S. L. Rumyantsev, C. Jiang, M. S. Shur, A. A. Balandin, *IEEE Electron Device Lett.* **2015**, *36*, 1202.
[108] A. R. Cadore, E. Mania, A. B. Alencar, N. P. Rezende, S. de Oliveira, K. Watanabe, T. Taniguchi, H. Chacham, L. C. Campos, R. G. Lacerda, *Sens. Actuators, B* **2018**, *266*, 438.
[109] H. K. Choi, J. Park, O. H. Gwon, J. Y. Kim, S.-J. Kang, H. R. Byun, B. Shin, S. G. Jang, H. S. Kim, Y.-J. Yu, *ACS Appl. Mater. Interfaces* **2022**, *14*, 23617.
[110] A. Ali, O. Koybasi, W. Xing, D. N. Wright, D. Varandani, T. Taniguchi, K. Watanabe, B. R. Mehta, B. D. Belle, *Sens. Actuators, A* **2020**, *315*, 112247.
[111] T. Georgiou, R. Jalil, B. D. Belle, L. Britnell, R. V Gorbachev, S. V Morozov, Y.-J. Kim, A. Gholinia, S. J. Haigh, O. Makarovsky, L. Eaves, L. A. Ponomarenko, A. K. Geim, K. S. Novoselov, A. Mishchenko, *Nat. Nanotechnol.* **2013**, *8*, 100.
[112] H. K. Choi, J. Park, N. Myoung, H. J. Kim, J. S. Choi, Y. K. Choi, C. Y. Hwang, J. T. Kim, S. Park, Y. Yi, S. K. Chang, H. C. Park, C. Hwang, C. G. Choi, Y. J. Yu, *Nanoscale* **2017**, *9*, 18644.
[113] Z. Feng, B. Chen, S. Qian, L. Xu, L. Feng, Y. Yu, R. Zhang, J. Chen, Q. Li, Q. Li, C. Sun, H. Zhang, J. Liu, W. Pang, D. Zhang, *2D Mater.* **2016**, *3*, 035021.
[114] S. Dhara, H. Jawa, S. Ghosh, A. Varghese, D. Karmakar, S. Lodha, *ACS Appl. Mater. Interfaces* **2021**, *13*, 30785.
[115] W. Zheng, Y. Xu, L. Zheng, C. Yang, N. Pinna, X. Liu, J. Zhang, *Adv. Funct. Mater.* **2020**, *30*, 2000435.
[116] H. Tabata, Y. Sato, K. Oi, O. Kubo, M. Katayama, *ACS Appl. Mater. Interfaces* **2018**, *10*, 38387.
[117] Y. Kim, S. Lee, J. G. Song, K. Y. Ko, W. J. Woo, S. W. Lee, M. Park, H. Lee, Z. Lee, H. Choi, W. H. Kim, J. Park, H. Kim, *Adv. Funct. Mater.* **2020**, *30*, 200360.
[118] L. Liu, N. Xu, Y. Zhang, P. Zhao, H. Chen, S. Deng, *Adv. Funct. Mater.* **2019**, *29*, 1807893.
[119] R. K. Jha, P. K. Guha, *IEEE Trans. Nanotechnol.* **2018**, *17*, 582.
[120] S. Y. Park, Y. H. Kim, S. Y. Lee, W. Sohn, J.-E. Lee, D. H. Kim, Y.-S. S. Shim, K. C. Kwon, K. S. Choi, H. J. Yoo, J. M. Suh, M. Ko, J.-H. Lee, M. J. Lee, S. Y. Kim, M. H. Lee, H. W. Jang, *J. Mater. Chem. A* **2018**, *6*, 5016.
[121] J. Shen, Z. Yang, Y. Wang, L.-C. Xu, R. Liu, X. Liu, *J. Phys. Chem. C* **2021**, *125*, 427.
[122] T. Hussain, M. Sajjad, D. Singh, H. Bae, H. Lee, J. A. Larsson, R. Ahuja, A. Karton, *Carbon* **2020**, *163*, 213.
[123] J. W. Jiang, H. S. Park, *Appl. Phys. Lett.* **2014**, *105*, 3.
[124] J. Y. Lin, G. Yue, S. Y. Tai, Y. Xiao, H. M. Cheng, F. M. Wang, J. Wu, *Mater. Chem. Phys.* **2013**, *143*, 53.
[125] N. A. Kumar, M. A. Dar, R. Gul, J. B. Baek, *Mater. Today* **2015**, *18*, 286.
[126] M. Pumera, *Chem. Soc. Rev.* **2010**, *39*, 4146.
[127] Y. Zhu, S. Murali, W. Cai, X. Li, J. W. Suk, J. R. Potts, R. S. Ruoff, *Adv. Mater.* **2010**, *22*, 3906.
[128] A. Ambrosi, C. K. Chua, A. Bonanni, M. Pumera, *Chem. Rev.* **2014**, *114*, 7150.
[129] H. Yang, J. Zhou, J. Bao, Y. Ma, J. Zhou, C. Shen, H. Luo, M. Yang, C. Hou, D. Huo, *Microchem. J.* **2021**, *162*, 105746.
[130] M. Govindasamy, V. Mani, S. M. Chen, R. Karthik, K. Manibalan, R. Umamaheswari, *Int. J. Electrochem. Sci.* **2016**, *11*, 2954.
[131] J. Hu, J. Zhang, Z. Zhao, J. Liu, J. Shi, G. Li, P. Li, W. Zhang, K. Lian, S. Zhuiykov, *Ionics* **2018**, *24*, 577.
[132] Y. Han, R. Zhang, C. Dong, F. Cheng, Y. Guo, *Biosens. Bioelectron.* **2019**, *142*, 111529.
[133] R. Madhuvilakku, S. Alagar, R. Mariappan, S. Piraman, *Anal. Chim. Acta* **2020**, *1093*, 93.
[134] K. J. Huang, L. Wang, J. Li, Y. M. Liu, *Sens. Actuators, B* **2013**, *178*, 671.
[135] N. Demir, K. Atacan, M. Ozmen, S. Z. Bas, *New J. Chem.* **2020**, *44*, 11759.
[136] M. H. M. Facure, R. Schneider, D. M. dos Santos, D. S. Correa, *Talanta* **2020**, *217*, 121039.
[137] H. Liu, X. Chen, X. Su, C. Duan, K. Guo, Z. Zhu, *J. Electrochem. Soc.* **2015**, *162*, B312.
[138] J. Yoon, T. Lee, B. Bapurao, J. Jo, B. K. Oh, J. W. Choi, *Biosens. Bioelectron.* **2017**, *93*, 14.
[139] T. D. F. Paulo, I. C. N. Diógenes, H. D. Abruña, *Langmuir* **2011**, *27*, 2052.
[140] A. B. Moghaddam, M. R. Ganjali, R. Dinarvand, S. Ahadi, A. A. Saboury, *Biophys. Chem.* **2008**, *134*, 25.
[141] J. Yoon, J. W. Shin, J. Lim, M. Mohammadniaei, G. Bharate Bapurao, T. Lee, J. W. Choi, *Colloids Surf., B* **2017**, *159*, 729.
[142] K. Zhang, H. Sun, S. Hou, *Anal. Methods* **2016**, *8*, 3780.

[143] O. Jalil, C. M. Pandey, D. Kumar, *Bioelectrochemistry* **2021**, *138*, 107733.
[144] K. Chang, W. Chen, *ACS Nano* **2011**, *5*, 4720.
[145] C. M. Pandey, G. Sumana, I. Tiwari, *Appl. Phys. Lett.* **2014**, *105*, 103706.
[146] J. M. Jeong, M. H. Yang, D. S. Kim, T. J. Lee, B. G. Choi, D. H. Kim, *J. Colloid Interface Sci.* **2017**, *506*, 379.
[147] Z. Wang, S. Dong, M. Gui, M. Asif, W. Wang, F. Wang, H. Liu, *Anal. Biochem.* **2018**, *543*, 82.
[148] F. Xu, M. Wu, G. Ma, H. Xu, W. Shang, *Microchem. J.* **2020**, *159*, 105432.
[149] J. Suh, T. L. Tan, W. Zhao, J. Park, D. Y. Lin, T. E. Park, J. Kim, C. Jin, N. Saigal, S. Ghosh, Z. M. Wong, Y. Chen, F. Wang, W. Walukiewicz, G. Eda, J. Wu, *Nat. Commun.* **2018**, *9*, 199.
[150] P. Luo, F. Zhuge, Q. Zhang, Y. Chen, L. Lv, Y. Huang, H. Li, T. Zhai, *Nanoscale Horiz.* **2019**, *4*, 26.
[151] L. Lan, Y. Yao, J. Ping, Y. Ying, *ACS Appl. Mater. Interfaces* **2017**, *9*, 23287.
[152] D. H. J. Bunka, P. G. Stockley, *Nat. Rev. Microbiol.* **2006**, *4*, 588.
[153] G. Seo, G. Lee, M. J. Kim, S. H. Baek, M. Choi, K. B. Ku, C. S. Lee, S. Jun, D. Park, H. G. Kim, S. J. Kim, J. O. Lee, B. T. Kim, E. C. Park, S. Il Kim, *ACS Nano* **2020**, *14*, 5135.
[154] G. S. Geleta, Z. Zhao, Z. Wang, *Analyst* **2018**, *143*, 1644.
[155] F. Chekin, K. Bagga, P. Subramanian, R. Jijie, S. K. Singh, S. Kurungot, R. Boukherroub, S. Szunerits, *Sens. Actuators, B* **2018**, *262*, 991.
[156] L. Tian, J. Qi, K. Qian, O. Oderinde, Y. Cai, C. Yao, W. Song, Y. Wang, *Sens. Actuators, B* **2018**, *260*, 676.
[157] L. Xing, Z. Ma, *Microchim. Acta* **2016**, *183*, 257.
[158] S. P. Figerez, K. K. Tadi, K. R. Sahoo, R. Sharma, R. K. Biroju, A. Gigi, K. A. Anand, G. Kalita, T. N. Narayanan, *Tungsten* **2020**, *2*, 411.
[159] K. D. Kıranşan, E. Topçu, *Electroanalysis* **2018**, *30*, 810.
[160] M. B. Hossain, M. M. Rana, *Sens. Lett.* **2016**, *14*, 145.
[161] A. K. Mishra, S. K. Mishra, R. K. Verma, *J. Phys. Chem. C* **2016**, *120*, 2893.
[162] A. Hoggard, L. Y. Wang, L. Ma, Y. Fang, G. You, J. Olson, Z. Liu, W. S. Chang, P. M. Ajayan, S. Link, *ACS Nano* **2013**, *7*, 11209.
[163] N. Reckinger, A. Vlad, S. Melinte, J. F. Colomer, M. Sarrazin, *Appl. Phys. Lett.* **2013**, *102*, 211108.
[164] J. Kim, H. Son, D. J. Cho, B. Geng, W. Regan, S. Shi, K. Kim, A. Zettl, Y. R. Shen, F. Wang, *Nano Lett.* **2012**, *12*, 5598.
[165] S. Zeng, S. Hu, J. Xia, T. Anderson, X. Q. Dinh, X. M. Meng, P. Coquet, K. T. Yong, *Sens. Actuators, B* **2015**, *207*, 801.
[166] M. K. S. Rahman, M. S. Anower, M. K. S. Rahman, M. R. Hasan, M. B. Hossain, M. I. Haque, *Optik* **2017**, *140*, 989.
[167] M. S. Rahman, M. S. Anower, M. R. Hasan, M. B. Hossain, M. I. Haque, *Opt. Commun.* **2017**, *396*, 36.
[168] S. Aksimsek, H. Jussila, Z. Sun, *Opt. Commun.* **2018**, *428*, 233.
[169] L. Wu, J. Guo, Q. Wang, S. Lu, X. Dai, Y. Xiang, D. Fan, *Sens Actuators, B* **2017**, *249*, 542.
[170] M. S. Rahman, M. S. anower, L. F. Abdulrazak, *Photonics Nanostructures: Fundam. Appl.* **2019**, *35*, 100711.
[171] B. H. Ong, X. Yuan, S. C. Tjin, J. Zhang, H. M. Ng, *Sens. Actuators, B* **2006**, *114*, 1028.
[172] M. El barghouti, A. Akjouj, A. Mir, *Opt. Laser Technol.* **2020**, *130*, 106306.
[173] J. B. Maurya, Y. K. Prajapati, V. Singh, J. P. Saini, *Appl. Phys. A: Mater. Sci. Process.* **2015**, *121*, 525.
[174] M. B. Hossain, M. M. Rana, L. F. Abdulrazak, S. Mitra, M. Rahman, *Biochem. Biophys. Rep.* **2019**, *18*, 100639.
[175] H. Yu, Y. Chong, P. Zhang, J. Ma, D. Li, *Talanta* **2020**, *219*, 121324.
[176] S. Chen, Y. Sun, Y. Xia, K. Lv, B. Man, C. Yang, *Biosens. Bioelectron.* **2020**, *156*, 112128.
[177] P. T. K. Loan, W. Zhang, C. T. Lin, K. H. Wei, L. J. Li, C. H. Chen, *Adv. Mater.* **2014**, *26*, 4838.
[178] F. Li, S. Wang, H. Yin, Y. Chen, Y. Zhou, J. Huang, S. Ai, *ACS Sens.* **2020**, *5*, 1092.

Hui-Lei Hou received his Ph.D. in analytical chemistry with Prof. Xiang Gao at Changchun Institute of Applied Chemistry, University of Chinese Academy of Sciences. He is currently a post-doctoral fellow at CIC biomagune in the Carbon Bionanotechnology Lab of Professor Maurizio Prato. His research focuses on new approaches for synthesizing 2D Heterostructures and the functionalization of low-dimensional carbon materials with various applications, such as SERS and drug delivery.

Cosimo Anichini received his M.Sc. in chemistry from the University of Bologna in 2016. Then, he joined the group of Prof. Samorì at the University of Strasbourg, where he was appointed Ph.D. in 2020. After one-year postdoctoral fellowship in the same group he is now research scientist at BeDimensional S.p.A. His research interest is focused on the development of multifunctional hybrid materials and composites based on 2D and other low-dimensional materials.

Paolo Samorì is distinguished professor at the University of Strasbourg and Director of the Institut de Science et d'Ingénierie Supramoléculaires. He is Member of the European Academy of Sciences and Arts, Fellow of the European Academy of Sciences (EURASC), Member of the Academia Europaea, Foreign Member of the Royal Flemish Academy of Belgium for Science and the Arts (KVAB) and Senior Member of the Institut Universitaire de France (IUF). His research interests comprise nanochemistry, supramolecular sciences, materials chemistry with specific focus on graphene and other 2D materials as well as functional organic/polymeric and hybrid nanomaterials for application in optoelectronics, energy and sensing.

Alejandro Criado received his BS degree in chemistry, followed by his Ph.D. in organic chemistry at the University of Santiago de Compostela. Then, he was a postdoctoral fellow at the University of Trieste and at CICbiomaGUNE. Currently, he is a Ramon y Cajal researcher at CICA – Universidade da Coruña, where he co-leads the NanoSelf group. His research interests focus on the new modification methods of low-dimensional materials to tailor their properties, along with the development of graphene-based sensors.

Maurizio Prato is Professor of Organic Chemistry at the University of Trieste and Ikerbasque Research Professor at CIC biomaGUNE, Spain. He is a member of the Italian Academy of Sciences (Accademia Nazionale dei Lincei), the Royal Spanish Academy of Sciences and the National Academy of Inventors (USA). His research focuses on the synthesis of novel functional materials, for applications in materials science and nanomedicine, which include spinal cord repair, splitting of water, and reduction of carbon dioxide into useful chemicals.